

# Continuous-Time RST Control of a Cart-Mounted Inverted Pendulum

Dev Kumar

▶ **To cite this version:**

Dev Kumar. Continuous-Time RST Control of a Cart-Mounted Inverted Pendulum. Independent research; original project at École Nationale Supérieure d'Arts et Métiers. 2026, pp.1-50. ⟨hal-05873003⟩

**HAL Id: hal-05873003**

**https://hal.science/view/index/docid/5873003**

Submitted on 19 Nov 2026

**HAL** is a multi-disciplinary open access archive for the deposit and dissemination of scientific research documents, whether they are published or not. The documents may come from teaching and research institutions in France or abroad, or from public or private research centers.

L'archive ouverte pluridisciplinaire **HAL**, est destinée au dépôt et à la diffusion de documents scientifiques de niveau recherche, publiés ou non, émanant des établissements d'enseignement et de recherche français ou étrangers, des laboratoires publics ou privés.



Copyright - All rights reserved

# Continuous-Time RST Control of a Cart-Mounted Inverted Pendulum

Sinusoidal tracking, stability margins and Python simulations

**Dev Kumar**

ORCID 0009-0008-2279-9163 · contact@dev-kumar.com

École Nationale Supérieure d'Arts et Métiers

Paris, France

**2026 engineering project**
Original material and reproducible numerical study

# Abstract

A cart-mounted inverted pendulum is stabilised and commanded to track a constant offset and a sinusoidal position reference using continuous-time RST control. This report reconstructs the 2026 design and identifies the conditions under which its frequency- and time-domain conclusions hold. It derives the mechanics and cart servo, solves the Bézout and feedforward coefficient equations, and compares the design model with a model that retains cart dynamics. At 0.35 m, the retuned phase margin drops from 42.8° to 33.3° when the cart servo is included. At 0.16 m it is 24.4°, corresponding to about 22 ms of additional pure delay. A polynomial imaginary-axis test establishes continuous-length linear stability in the nominal servo model over 0.16–0.35 m. The reconstructed reference remains inside the ±5 V command interval. A separate 0.40 V measurement pulse produces 7.02 V of demand with the retuned controller. Additional experiments quantify frequency detuning, the effect of disturbance location, and the dependence of finite-angle trajectories on saturation and sensor calibration. The archived Simulink figures and the reproducible Python comparisons support distinct, explicitly identified findings.


**Keywords** inverted pendulum, RST, internal model, polynomial pole placement, Nyquist criterion, actuator saturation.

### Study record

Source [1] is the 37-page 2026 engineering report. Its original graphs appear at the point of analysis. Source page references use the physical PDF page numbers, including the cover. New figures and numerical tables are generated by the companion Python script.


### Acknowledgement

The author thanks Hervé Guillard for supervising the original project at École Nationale Supérieure d’Arts et Métiers.


# Nomenclature

| Symbol | Meaning |
|---|---|
| $x$, $x_b$, $L$, $\theta$ | Cart position, geometric tip position, pendulum length, upright angle |
| $M$, $m$, $f$, $g$ | Cart mass, point mass, horizontal applied force, gravitational acceleration |
| $\lambda$, $\alpha$, $\omega_0$ | $g/L$, positive pendulum pole $\sqrt{\lambda}$, reference angular frequency |
| $K_x$, $x_m$, $\eta$ | Cart voltage scale, scaled cart position, scaled angle contribution |
| $r$, $u$, $u_a$ | Reference, outer-loop demand, applied outer command |
| $y$, $z$, $d_u$, $d_o$, $b$ | Output before sensor corruption, measured output, input and output disturbances, sensor corruption |
| $D_c$, $H_1$, $H_2$ | Cart denominator, cart servo and reduced pendulum transfer |
| $\zeta$, $\omega_c$, $\omega_d$ | Cart damping ratio, natural and damped angular frequencies |
| $A$, $B$, $P$, $R$, $S$, $T$ | Plant and characteristic polynomials, RST controller polynomials |
| $\beta$, $\gamma$, $k$, $\tau$ | Design pole rates, gain multiplier, added pure delay |
| $\sigma$, $\omega_g$, $\varphi_m$, $M_m$ | Spectral abscissa, unity-gain frequency, phase margin, modulus margin |

# Contents


Abstract 1
Study record 1
Acknowledgement 1
Nomenclature 1
1 Research questions and evidence 3
1.1 Control problem 3
1.2 Questions and comparison design 3
1.3 Source availability and numerical status 4
1.4 Structure of the evidence 4
2 RST framework for sinusoidal tracking 4
2.1 Complex steady-state argument 4
2.2 Two-degree-of-freedom architecture 5
2.3 Enforcing the internal model 5
2.4 Degree count 6
2.5 Bézout solvability and uniqueness 6
3 Cart–pendulum mechanics and model identification 6
3.1 Coordinates and energy 6
3.2 Linearization and sign audit 7
3.3 Local position servo 8
3.4 Readings from the cart experiment 9
3.5 From two sensors to the controlled coordinate 10
3.6 Reduced and retained plants 11
3.7 Frequency range of the servo approximation 11
4 Continuous-time controller synthesis 12
4.1 Nominal design assumptions 12
4.2 Choice and expansion of the pole product 12
4.3 Matching the Bézout coefficients 13
4.4 Feedforward interpolation 14
5 Frequency-domain verification 16
5.1 Definitions and asymptotes 16
5.2 Reading the original Bode curves 17
5.3 Algebraic crossovers and stable gain intervals 17
5.4 Generalized Nyquist count 18
5.5 Modulus margin and peak sensitivity 19
5.6 An additional transport-delay threshold 20
6 Reading the archived Simulink curves 21
6.1 Signal routing and command sequence 21
6.2 Initial tuning 21
6.3 Retuned trace and correction of an angle reading 22
6.4 Original four-length comparison 23
7 Robustness to length, cart dynamics and retuning 24
7.1 Continuous length as a polynomial parameter 24
7.2 Root motion and repeated poles 24
7.3 The length sweep is sensitive to plant order 25
7.4 Joint uncertainty in the identified servo 26
7.5 Reassessment of the original pole-allocation strategy 26
8 Reproducible linear and limited-command experiments 28
8.1 State model, time grid and metrics 28
8.2 E1: Reconstructed reference without an added disturbance 28
8.3 E2: Independent cart-input pulse 30
8.4 E3: Independent measurement pulse 31
8.5 E4: Robustness to frequency detuning 32
9 Finite-angle response and calibration dependence 34
9.1 Pendulum equation with the identified cart 34
9.2 What the archived angles imply for the approximation 34
9.3 E5: Initial-angle experiments with the command limit 35
9.4 Scaling the finite-angle test 36
10 Interpretation and experimental checks 37
10.1 What the comparisons establish 37
10.2 Limiting assumptions 37
10.3 From a continuous delay margin to a sampled model 37
10.4 Model comparison protocol 38
11 Conclusion 38
References 39
A Controller coefficients and shared realisation 39
A.1 Complete polynomial coefficients 39
A.2 Why the two inputs share controller states 39
A.3 Parallel roles of the original MATLAB steps 40
B Reproducing the numerical results 40
B.1 Running the companion script 40
B.2 Integration checks 41
B.3 Checking a result from the polynomials alone 41
C Original figure concordance 42
D Original equations and numerical statements 43
E Original MATLAB listings 47

# 1 Research questions and evidence

## 1.1 Control problem

The 2026 project [1] uses a motorised cart to stabilise a pendulum about its upright equilibrium and track a sinusoidal position reference. Near upright, the hanging mass moves horizontally in response to both cart displacement and pendulum deflection. The controlled signal combines these two contributions. The position of the cart itself, the pendulum angle and the combined voltage-coordinate output are distinct quantities. Keeping them distinct matters when a narrow tracking error coexists with a large angle or significant cart travel.

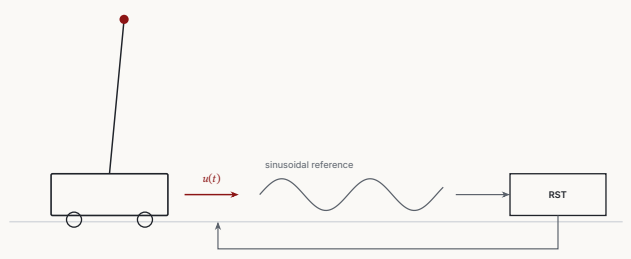


**Figure 1.1** – Original cover sketch of the pendulum, sinusoidal command and feedback loop [1, PDF p. 1].

The design operates on two levels. A local cart-position servo uses position and velocity feedback. A continuous-time RST controller commands that servo and receives the combined measurement. The original design approximates the cart servo by its static gain during outer-loop synthesis. The approximation keeps the unstable pendulum mode and makes the Bézout calculation explicit. Its accuracy near the reference frequency can differ markedly from its accuracy at the frequencies that determine margins.

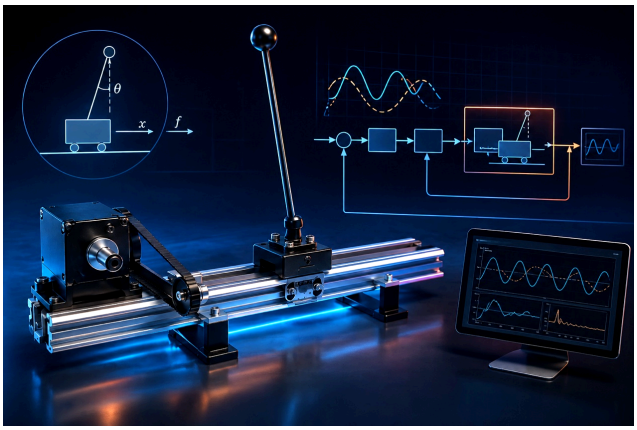

**Figure 1.2** – Conceptual illustration of the platform and sinusoidal tracking from the original Executive Summary [1, PDF p. 3]. The measured and simulated trajectories are identified by source figure in Appendix C.

The problem also separates steady-state tracking from transient authority. The internal model permits asymptotically exact tracking of a constant and one sinusoidal frequency in the stable linear model. A finite command limit introduces a separate feasibility condition. A short measurement pulse, an input disturbance, a change in the reference and an initial angular offset can expose different parts of that condition even if they produce superficially similar output plots.

## 1.2 Questions and comparison design

The first question is whether the signed model and polynomial coefficients can be recovered from the equations, block diagrams and console output of the original. The analysis checks the signs in the mechanical derivation, translates the source's gain conventions and computes each RST coefficient from the target pole product. The comparison uses the initial setting $\beta = 1$, $\gamma = 10$ and the reported retuning $\beta = 0.5$, $\gamma = 30$. Both are synthesised at $L = 0.35$ m with reference frequency 1 rad/s.

The second question is what changes when the cart pole pair is retained. For that comparison the RST coefficients and length are held fixed while the plant model alone is changed. The frequency analysis checks characteristic roots, algebraic crossover equations, modulus margin and an oriented Nyquist count. With one controller held

fixed, an affine polynomial in g/L checks the continuous length interval. A separate discrete grid probes variation in the estimated servo frequency and damping ratio. These are different uncertainty sets and support different claims.

The third question concerns transient performance. The archived reference can be reconstructed approximately from the time traces. The source describes a disturbance near 15 s, and its graphs also show a change in the reference at that time. The reconstruction uses the visible reference alone, followed by independent tests with explicitly specified perturbations at the servo input and the measured output. An additional periodic test changes the reference frequency while preserving the designed RST coefficients. Finite-angle runs restore the sine and cosine terms and vary an assumed calibration to identify which conclusions depend on the command scale.

### 1.3 Source availability and numerical status

The archive is a report with legible diagrams, screenshots and MATLAB extracts. It names `TP2_RST_Pendule_Dev_KUMAR.m`, `simu_rst_pendule.mdl` and `placement_poles.py`. Executable copies and the original records of sampled time series were unavailable. The archived identification trace supplies the servo assumptions. Time-domain cursor readings support comparisons at the plotted points. They provide limited information about unlogged settings and uncertainty.

The independent computations use signals in voltage coordinates. The distinction between outer command and motor drive is maintained throughout. The ±5 V criterion refers to the simulated outer command because the original report plots that signal against the bounds. The physical voltage-to-displacement relation needed to express angle and travel numerically is treated as an explicit scenario parameter. No experimental claim is assigned to the Python time histories.

### 1.4 Structure of the evidence

The mathematical argument proceeds from tracking conditions to a reduced and an augmented plant, then to the controller. The associated diagrams appear beside the derivations. Closed-loop poles and frequency curves supply the first model comparison. Archived tracking, command and angle plots are read before the new simulations are interpreted. The last sections state the model adequacy checks, the quantities needed for experimental validation and the steps to reproduce the new tables and figures. Appendix C links the original figure numbers to the same panels in the manuscript. Appendices D and E reproduce the original equations and MATLAB listings.

## 2 RST framework for sinusoidal tracking

### 2.1 Complex steady-state argument

Let G be a strictly stable linear transfer and let the input be a sinusoid of amplitude a and positive angular frequency $\omega_0$. A complex input a exp(j$\omega_0$t) makes the sinusoidal steady-state argument direct. For a causal impulse response $g_G$ and zero initial state the output is a convolution. Substituting t-τ in the input yields an integral whose limit is the Fourier transform of the impulse response, evaluated at $\omega_0$.

$$v(t) = a e^{j\omega_0 t} \int_0^t g_G(\tau) e^{-j\omega_0 \tau}\, d\tau$$
$$v_{ss}(t) = a G(j\omega_0) e^{j\omega_0 t} \tag{2.1}$$

The response to the real sine is the imaginary part of this expression. If an initial state is present, exponential stability ensures its contribution tends to zero. For perfect sinusoidal tracking by a closed-loop transfer $G_r$, the amplitude ratio must be one and the phase must be zero modulo 2π. Equivalently, the error transfer $G_r$-1 must vanish at j$\omega_0$. With real coefficients the conjugate frequency imposes the corresponding conjugate condition automatically.

$$e_{ss}(t) = a\,\mathrm{Im}\{[G_r(j\omega_0) - 1] e^{j\omega_0 t}\}$$
$$e_{ss} \equiv 0 \iff G_r(j\omega_0) = 1 \tag{2.2}$$

The same result follows from the residue at the two poles of a sinusoidal input transform. Multiplying by an error transfer with zeros at the input poles removes the forced oscillatory terms. For a step input the real-axis counterpart is $G_r(0)=1$, provided the remaining error dynamics decay. These conclusions require a stable *closed* loop. A phase-amplitude reading of an unstable plant alone cannot be interpreted as its long-time response to a sine.

## 2.2 Two-degree-of-freedom architecture

Use B/A for the plant and R,S,T for the continuous-time controller polynomials. Write r for the reference, y for the output before measurement corruption, z for the measured output and u for the outer-loop command. The Laplace transform of r is $R_f$, distinct from the polynomial R. The original diagram in Figure 2.1 identifies the three disturbance locations. Here $d_u$ acts at the plant input, $d_o$ adds to the physical output and b adds in the sensor.

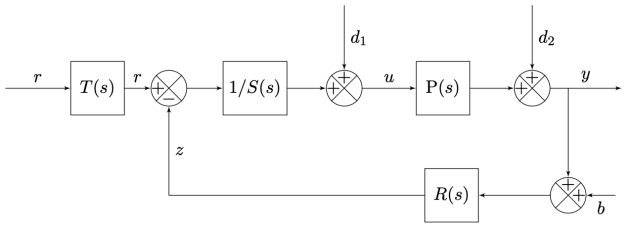


**Figure 2.1** – Original RST architecture [1, PDF p. 8]. The source labels the two plant disturbances $d_1$ and $d_2$. For this section they are $d_u$ and $d_o$. The measurement block adds b. Original Fig. 2.1.

$$\begin{aligned} AY &= B(U+D_u)+AD_o \\ Z &= Y+N_b, \qquad SU = TR_f - RZ \\ P &= AS+BR \end{aligned} \tag{2.3}$$

Here $N_b$ denotes the transform of the sensor term. Multiply the plant equation by S and substitute the controller. The term -BRY moves to the left and forms the characteristic polynomial. Adding P $N_b$ to PY gives the measured-output relation, using P-BR=AS. Eliminating Y from the controller similarly yields the command relation. The resulting four channels for each output are as follows.

$$\begin{aligned} PY &= BTR_f + BSD_u + ASD_o - BRN_b \\ PZ &= BTR_f + BSD_u + AS(D_o+N_b) \\ PU &= ATR_f - BRD_u - AR(D_o+N_b) \end{aligned} \tag{2.4}$$

The reference transfer is BT/P, and the transfer from sensor corruption to physical output is -BR/P. The same sensor signal enters measured output through AS/P. Thus small measured error can coexist with a physical output excursion. This follows directly from the point of injection. The ratio from a physical output disturbance to y is AS/P, whereas a plant-input disturbance is filtered by BS/P. These two transfers differ by the plant.

Feedback contributes R/S to the characteristic equation. The reference path T/S supplies a second design degree of freedom. Changing T does not change the linear characteristic polynomial, since T multiplies only the independent reference. Large command values still depend on T because the feedforward path can pass a reference step directly through its leading coefficient. This distinction becomes important when reading the three traces in a reference experiment.

## 2.3 Enforcing the internal model

Set $G_r$=BT/P and define E=Y-$R_f$ in the absence of disturbances. Then

$$\frac{E}{R_f} = \frac{B(T-R)-AS}{AS+BR}. \tag{2.5}$$

Vanishing of this numerator at $s=j\omega_0$ is the single nominal tracking condition. The 2026 synthesis meets it by imposing two sufficient conditions, $S(j\omega_0)=0$ and $T(j\omega_0)=R(j\omega_0)$. This choice has a stronger consequence than a nominal cancellation in the numerator: when $S(s_0)=0$ and the perturbed plant still has $B(s_0)R(s_0)\neq 0$, the tracking ratio stays one at $s_0$. This is the internal-model property used here [2]. The condition on the closed-loop poles remains essential.

$$\begin{aligned} F_i(s) &= s(s^2+\omega_0^2), \qquad S = F_iQ \\ s_0 &\in \{0, j\omega_0, -j\omega_0\}, \quad T(s_0)=R(s_0) \end{aligned} \tag{2.6}$$

At these roots P=BR and BS/P=AS/P=0. A disturbance input or additive physical-output signal

in the modelled class is rejected after transients under the stated stability condition. At the same frequencies sensor corruption is transferred with gain -1 to y and with gain zero to z. This relation explains why a sensor bias must be distinguished from a force or voltage perturbation. It also gives a reason to retain a separate raw measurement channel during bench tests.

$$\begin{gathered}\frac{Y}{R_f}=1,\quad \frac{Y}{D_u}=\frac{Y}{D_o}=0\\ \frac{Y}{N_b}=-1,\quad \frac{Z}{N_b}=0\\ \text{at } s=s_0\end{gathered}\tag{2.7}$$

A branch T/S with poles on the imaginary axis is consistent with internal closed-loop stability when those modes appear in the single feedback realisation. Implementing two independent integrators for the two paths can introduce redundant states whose modes are not represented in P. Appendix A derives a shared realisation which avoids this ambiguity. The use of polynomials in s is explicitly continuous-time. Reference [3] describes the related digital R–S–T architecture.

### 2.4 Degree count

Take a monic A of degree n and deg B < n. Let k = deg R and δ = deg S − deg R ≥ 0. Causal proper realisation requires deg R, deg T ≤ deg S. Write the monic polynomial Q in equation (2.6) with degree k + δ − 3. There are k + 1 unknown R coefficients and k + δ − 3 unknown Q coefficients after its monic leading term is fixed. Because AS has the larger degree, P is monic of degree n + k + δ.

$$\begin{gathered}N_u=(k+1)+(k+\delta-3)\\ N_e=n+k+\delta\\ N_e=N_u \implies k=n+2\end{gathered}\tag{2.8}$$

The number n+2 comes from the three imposed modes 0 and $\pm j\omega_0$. With an arbitrary internal model of degree $m_i$, the same count gives $k=n+m_i-1$. Degree counting identifies how many coefficients can be specified. A solvability condition is needed to ensure that the equations are independent.

### 2.5 Bézout solvability and uniqueness

Set $A_i=AF_i$. The target equation becomes $A_iQ+BR=P_\star$. Suppose $A_i$ and B are coprime. The Euclidean algorithm then supplies a polynomial J with JB=1 modulo $A_i$. Take R to be the remainder of $JP_\star$ after division by $A_i$. It has degree strictly below deg $A_i$=n+3, which matches the upper bound n+2 from equation (2.8). Define Q by the remaining quotient. The numerator is divisible by $A_i$, and its monic degree implies Q is monic with the desired degree.

$$\begin{gathered}R\equiv JP_\star \pmod{A_i}\\ Q=\frac{P_\star-BR}{A_i},\\ JB\equiv 1 \pmod{A_i}\end{gathered}\tag{2.9}$$

For uniqueness consider the difference of two solutions. The coprimeness assumption implies $A_i$ divides their R difference, while its degree is strictly below deg $A_i$. Therefore the difference is zero, and the Q difference is zero as well. A common plant numerator zero at an internal-model frequency would remove the required inverse and invalidate this argument. In the design plant below, B is a nonzero constant, so the coprimeness condition is immediate.

$$\begin{gathered}A_i\Delta Q=-B\Delta R,\\ A_i\mid\Delta R,\quad \deg\Delta R<\deg A_i\\ \Delta R=0,\quad \Delta Q=0\end{gathered}\tag{2.10}$$

# 3 Cart–pendulum mechanics and model identification

### 3.1 Coordinates and energy

The cart has mass M and translates horizontally by x. The pendulum is represented by a point mass m at distance L from the pivot on a rigid massless link. The angle θ is measured from the upward vertical towards positive x. With the pivot level used as the height origin, the moving mass lies at the coordinates in equation (3.1). A positive small angle places the bob to the right of the pivot. The gravitational potential is highest at upright.

$$x_b = x + L\sin\theta, \qquad z_b = L\cos\theta$$
$$\dot{x}_b = \dot{x} + L\dot{\theta}\cos\theta \tag{3.1}$$
$$\dot{z}_b = -L\dot{\theta}\sin\theta$$

Using these velocities in the sum of cart and pendulum kinetic energy eliminates the mixed sine-square and cosine-square terms. Only the horizontal velocity creates a cross term. Gravity is included through the potential energy. The external force f acts in x and the pivot is treated as frictionless.

$$\mathcal{T} = \frac{M+m}{2}\dot{x}^2 + mL\dot{x}\dot{\theta}\cos\theta + \frac{mL^2}{2}\dot{\theta}^2$$
$$\mathcal{V} = mgL\cos\theta, \tag{3.2}$$
$$\mathcal{L} = \mathcal{T} - \mathcal{V}$$

For the translational equation, the two contributions to the generalized momentum are the total translational momentum and the pendulum's relative horizontal momentum. The Lagrangian is independent of x. For the angular equation, the term containing the product of velocities appears in both the time derivative of the momentum and the derivative with respect to angle. These contributions cancel.

$$\frac{\partial \mathcal{L}}{\partial \dot{x}} = (M+m)\dot{x} + mL\dot{\theta}\cos\theta$$
$$\frac{\partial \mathcal{L}}{\partial \dot{\theta}} = mL\dot{x}\cos\theta + mL^2\dot{\theta} \tag{3.3}$$
$$\frac{\partial \mathcal{L}}{\partial \theta} = -mL\dot{x}\dot{\theta}\sin\theta + mgL\sin\theta$$

Euler–Lagrange with generalized forces f and zero gives the coupled equations. The sign of g in the second equation is fixed by the upright angle: for a motionless cart and a small positive θ, the angular acceleration is positive. A positive cart acceleration has the opposite effect near upright.

$$(M+m)\ddot{x} + mL\ddot{\theta}\cos\theta - mL\dot{\theta}^2\sin\theta = f$$
$$L\ddot{\theta} = g\sin\theta - \ddot{x}\cos\theta \tag{3.4}$$

Eliminating angular acceleration by substitution gives an inertial denominator $M+m\sin^2\theta$, strictly positive for $M > 0$. This denominator is the Schur complement of the angular inertia $mL^2$ in the two-coordinate mass matrix. The same equations give an energy consistency check: multiplying the translation equation by $\dot{x}$ and the angular equation by $mL\dot{\theta}$ and adding produces the derivative of T+V.

$$\ddot{x} = \frac{F_x}{M + m\sin^2\theta}$$
$$F_x = f - mg\sin\theta\cos\theta + mL\dot{\theta}^2\sin\theta \tag{3.5}$$
$$\frac{d}{dt}(\mathcal{T}+\mathcal{V}) = f\dot{x}$$

Equations (3.4)–(3.5) describe a force-driven benchmark. A physical simulation of that benchmark requires M, m and a conversion from drive and velocity to horizontal force. The archival servo fit provides an alternative description of cart acceleration seen by the pendulum. The retained-servo simulations below preserve that approximation and therefore omit the reaction force from the moving bob.

## 3.2 Linearization and sign audit

At rest, linearization of the gravity term uses $\sin\theta \approx \theta$ and the acceleration projection uses $\cos\theta \approx 1$. The velocity-square term is higher order about this rest equilibrium. The resulting angular equation is $L\theta = g\theta - \ddot{x}$. The printed small-angle and intervening Laplace equations in [1, PDF p. 11] reverse the gravitational and cart-acceleration terms. The source's subsequent block $s^2/(g - Ls^2)$ agrees with the corrected equation.

$$
\begin{aligned}
(M+m)\ddot{x} + mL\ddot{\theta} &= f \\
L\ddot{\theta} &= g\theta - \ddot{x} \\
\frac{\Theta(s)}{X(s)} & \\
= \frac{s^2}{g - Ls^2} &= -\frac{s^2}{L(s^2-\lambda)} \\
\lambda = \frac{g}{L}, \quad \alpha &= \sqrt{\lambda}
\end{aligned}
\tag{3.6}
$$

The ratio in equation (3.6) takes cart position as an independent input and assumes zero initial conditions. The mechanical coupling back into the cart follows from solving the first equation in Laplace form. The factor of $s^2$ from angular acceleration cancels the cart integrator pair in the coupling term. The coupling block is therefore static in this representation. An extra $s^{-2}$ in a printed intermediate expression would change that conclusion.

$$
\begin{aligned}
X(s) &= G_1(s)F(s) + G_2(s)\Theta(s) \\
G_1(s) &= \frac{1}{(M+m)s^2}, \\
G_2(s) &= -\frac{mL}{M+m} \\
G_3(s) &= \frac{\Theta(s)}{X(s)} \\
&= \frac{s^2}{g - Ls^2}
\end{aligned}
\tag{3.7}
$$

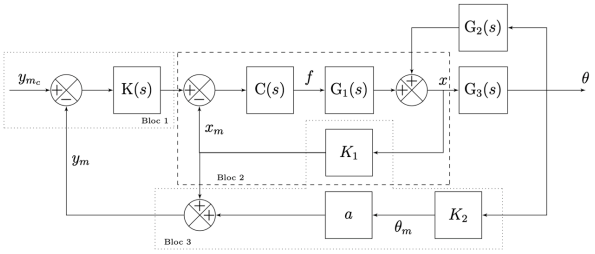


**Figure 3.1** – Original cart–pendulum architecture [1, PDF p. 11]. $G_1$ acts from force to cart position and $G_2$ is the pendulum reaction into the cart-position path. $G_3$ acts from cart position to angle. Original Fig. 3.1.

A useful check is to eliminate x from the coupled force-driven linear model rather than assume its acceleration is controlled ideally. Write $\lambda_f=(1+m/M)\lambda$. The force drives two cart integrators and an unstable pendulum pair with this modified rate. The force-to-cart transfer has zeros at $\pm\sqrt{\lambda}$; the ratio from prescribed displacement to angle in equation (3.6) does not contain the inertial factor 1+m/M. This calculation specifies which plant is being used when quoting an unstable pole.

$$
\begin{aligned}
M\ddot{x} &= f - mg\theta, \\
\ddot{\theta} &= \lambda_f\theta - \frac{f}{ML} \\
\frac{\Theta}{F} &= -\frac{1}{ML(s^2-\lambda_f)} \\
\frac{X}{F} &= \frac{s^2-\lambda}{Ms^2(s^2-\lambda_f)}
\end{aligned}
\tag{3.8}
$$

For fixed positive masses the force-driven system has a positive pole at $\sqrt{\lambda_f}$. The reduced plant in the design instead has a positive pole $\alpha = \sqrt{\lambda}$. Using the servo removes the need to estimate f in voltage-coordinate simulations. It does not make the force-driven and servo-based systems identical. Identification of the servo under pendulum loading would be required to quantify the feedback effect of $G_2$.

## 3.3 Local position servo

The modified cart servo in Figure 3.2 acts on the local command $x_{mc}$. Its actuator command $u_m$ is distinct from the outer-loop demand u used by the RST. Let $x_m=K_1 x$ and write $v_x=sX$. Denote the first-order motor velocity transfer by $K_m/(1+\tau_m s)$, and write $K_d K_3$ for the effective velocity-feedback gain. The source uses this inner structure before estimating the combined second-order closed loop.

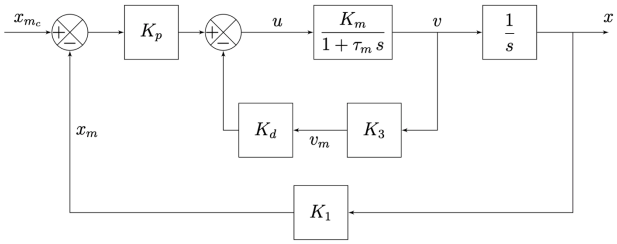


**Figure 3.2** – Original position servo [1, PDF p. 12]. The proportional position and velocity-feedback paths act before the first-order motor. The outer RST is outside this loop. Original Fig. 3.2.

$$
\begin{aligned}
U_m &= K_p(X_{mc} - X_m) - K_d K_3 V_x \\
(1+\tau_m s)V_x &= K_m U_m \\
V_x &= sX, \quad X_m = K_1 X
\end{aligned}
\tag{3.9}
$$

Substituting $U_m$ and collecting all terms in X produces a second-order denominator. Multiplication by $K_1$ converts the result from displacement to the measured cart coordinate. The constant term of this denominator also appears in the numerator, so this ideal inner structure predicts unit DC gain with positive proportional loop gain.

$$\begin{aligned}[\tau_m s^2 + (1 + K_m K_d K_3)s + K_m K_p K_1]X \\ = K_m K_p X_{mc} \\ H_1(s) = \frac{X_m}{X_{mc}} \\ = \frac{K_m K_p K_1}{\tau_m s^2 + (1 + K_m K_d K_3)s + K_m K_p K_1}\end{aligned} \tag{3.10}$$

Normalizing by $K_m K_p K_1$ gives the canonical form used in the computations. A measurement of the transfer determines combined coefficients. It cannot separately identify all motor and feedback gains in equation (3.10). No values for these individual parameters are needed by the cascade simulation.

$$\begin{aligned}D_c(s) = 1 + \frac{2\zeta}{\omega_c}s + \\ \frac{s^2}{\omega_c^2}, \qquad H_1 = D_c^{-1} \\ \omega_c = \sqrt{\frac{K_m K_p K_1}{\tau_m}} \\ \zeta = \frac{1 + K_m K_d K_3}{2\sqrt{\tau_m K_m K_p K_1}}\end{aligned} \tag{3.11}$$

## 3.4 Readings from the cart experiment

The reported excitation is a 1.5 Hz square wave with levels −0.25 and +0.25 V [1, PDF pp. 13–14]. Figure 3.3 preserves the plotted output after one transition. The two quasi-steady levels support a static gain near one. The full excitation is periodic, so this gain estimate relies on the plateaux within each half-cycle. The final-value theorem applies to the isolated-step model used to interpret those plateaux.

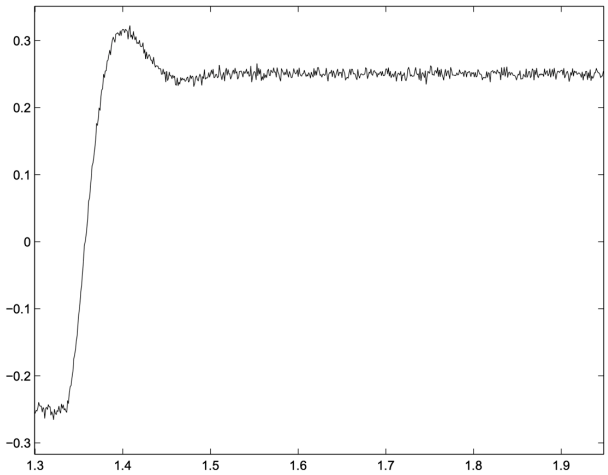


**Figure 3.3** – Archived local cart response [1, PDF p. 13]. The nominal positive plateau is about 0.25 V. The first maximum and next minimum are near 0.31 and 0.24 V. Original Fig. 3.3.

The underdamped unit-gain response from the lower level to the upper level has the form in equation (3.12) when it starts at steady rest. If t is measured from the switching instant, the first two extrema are at $\pi/\omega_d$ and $2\pi/\omega_d$. Their deviations from the upper plateau have opposite signs. Setting $a=\zeta\omega_c$ and starting from a 0.50 V step gives the exponential ratio in equation (3.13).

$$\begin{aligned}\omega_d = \omega_c\sqrt{1-\zeta^2}, \quad a = \zeta\omega_c \\ x_m(t) = 0.25 - 0.50e^{-at} \\ \left(\cos\omega_d t + \frac{a}{\omega_d}\sin\omega_d t\right)\end{aligned} \tag{3.12}$$

$$\begin{aligned}\Delta t = t_2 - t_1 = \frac{\pi}{\omega_d} \\ \frac{|x_2 - x_\infty|}{|x_1 - x_\infty|} \\ = e^{-\pi\zeta/\sqrt{1-\zeta^2}}\end{aligned} \tag{3.13}$$

With peaks reported at 1.41 and 1.48 s, $\Delta t=0.07$ s, the deviations are approximately 0.06 and 0.01 V. The logarithmic decrement for opposite peaks is ln 6. This estimates a half-period, rather than the full-period decrement used for peaks on the same side. The nominal identified values agree with the source within rounding.

$$\begin{aligned}\delta &= \ln\frac{0.31-0.25}{0.25-0.24} = \ln 6\\ \zeta &= \frac{\delta}{\sqrt{\pi^2+\delta^2}} \simeq 0.49542\\ \omega_c &= \frac{\pi}{0.07\sqrt{1-\zeta^2}}\\ &\simeq 51.6661 \text{ rad/s}\end{aligned} \tag{3.14}$$

The original report expresses the peak deviations as 24% and 4% of the positive plateau. Their ratio is correct for the decrement calculation. A single-edge overshoot formula uses the full step height. The first overshoot alone would be 0.06/0.50 = 12%, giving $\delta = -\ln 0.12$, $\zeta \approx 0.559$ and, with the same $\omega_d$, $\omega_c \approx 54.14$ rad/s. This difference is observable in Figure 3.4. The peak-ratio fit gives the right ratio 6 but predicts first and second peaks of 0.333 and 0.236 V for the ideal step. The first-peak fit gives 0.310 and 0.243 V. The readings and the single second-order approximation do not determine an exact servo transfer.

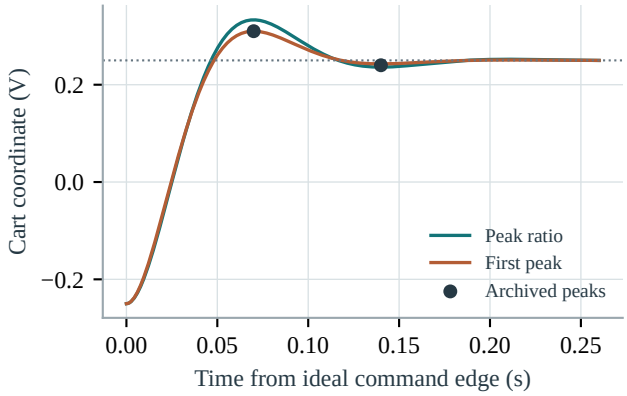


**Figure 3.4** – Calculated step responses for the two ways of using the archived extrema. Sample markers are placed at the inferred half-periods measured from a shared ideal edge. No sampled waveform was fit.

The second deviation is small, so a few millivolts of reading error can alter the damping estimate. First-order sensitivity of the decrement to the second peak is about 100 $V^{-1}$ at the displayed values. If both deviations and the time interval are taken from the original image, uncertainty in the inferred plateau and sample times contributes as well. Section 7 uses explicit test ranges for $\zeta$ and $\omega_c$. Those ranges should be understood as engineering perturbations, since a calibrated confidence interval would require repeated records.

$$\begin{aligned}\frac{\partial\delta}{\partial x_2} &= \frac{1}{x_\infty - x_2},\\ \frac{d\zeta}{d\delta} &= \frac{\pi^2}{(\pi^2+\delta^2)^{3/2}}\end{aligned} \tag{3.15}$$

## 3.5 From two sensors to the controlled coordinate

The measurement architecture uses gain $K_1$ on x and gain $K_2$ on θ, then weights the angular channel by a factor a. In this subsection call that factor $a_\theta$ to distinguish it from the decay rate in equation (3.12). Matching $K_1(x+L\theta)$ coefficient by coefficient gives $a_\theta = K_1 L/K_2$. Define $K_x = K_1$, $x_m = K_x x$ and $\eta = K_x L\theta$. The controller receives the sum $y = x_m + \eta$, with the additive sensor term included separately when needed.

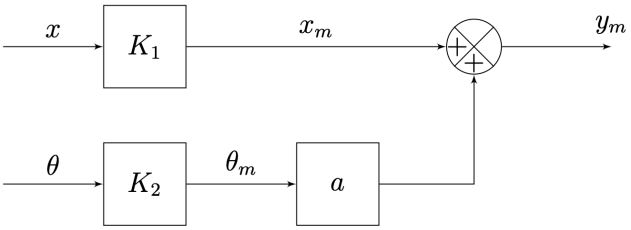


**Figure 3.5** – Original sensor mixing [1, PDF p. 14]. The angular sensor gain $K_2$ and weight a determine the coefficient of θ in the measured sum. Original Fig. 3.4.

$$\begin{aligned}y &= K_1 x + a_\theta K_2 \theta\\ a_\theta &= \frac{K_1 L}{K_2},\\ y &= x_m + \eta, \quad \eta = K_x L\theta\end{aligned} \tag{3.16}$$

The physical bob coordinate is $x_b = x + L\sin\theta$. The linear combination in equation (3.16) approximates $K_x x_b$ at small θ. The full geometric error is $K_x L(\theta - \sin\theta)$. Restoring the mechanics' trigonometric terms in a simulation leaves this signal convention intact. An encoder and cart calibration are needed to verify how the real sensors implement the combination.

$$\begin{aligned}y - K_x x_b &= K_x L(\theta - \sin\theta)\\ |y - K_x x_b| &\le \frac{K_x L}{6}|\theta|^3\end{aligned} \tag{3.17}$$

The numeric Simulink labels include 0.24, 0.53 and a length-dependent gain. They show how the two channels were scaled in the archived model. Available labels and plots do not fix a physical V/m conversion across the reconstructed scenarios. For the new angle and travel calculations $K_x$=24 V/m is a declared scenario value. The linear output response in volts follows directly from the transfer functions and cancels this scale.

## 3.6 Reduced and retained plants

After neglecting the reaction path $G_2$ the cart servo and angular relation form a cascade, shown in Figures 3.6 and 3.7. The ratio $y/x_m$ equals $1+L\,G_3$. The cancellation of the $s^2$ terms in the numerator yields unit DC gain for the reduced plant, one stable and one unstable real pole, and no finite zero. This is the second-order model $H_2$ in the design equation. Keeping the cart servo gives the fourth-order model $H_4=H_1H_2$.

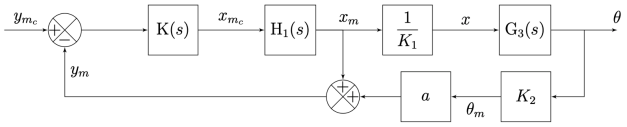


**Figure 3.6** – Original architecture with the cart reaction omitted [1, PDF p. 15]. The servo response sets the displacement entering the pendulum dynamics. Original Fig. 3.5.

$$\begin{aligned} H_2(s) &= 1 + LG_3(s) \\ &= \frac{g}{g - Ls^2} = \frac{-\lambda}{s^2 - \lambda} \\ H_4(s) &= H_1(s)H_2(s) = \frac{H_2(s)}{D_c(s)} \end{aligned} \tag{3.18}$$

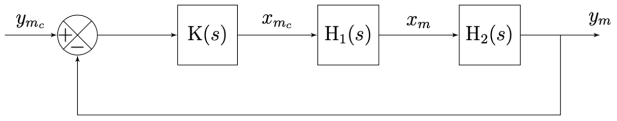


**Figure 3.7** – Equivalent cascade in the original study [1, PDF p. 15]. The implemented RST replaces the single feedback block drawn schematically in the source. Original Fig. 3.6.

A useful identity follows by differentiating $y=x_m+\eta$ twice in the linear model. The cart-acceleration terms cancel and the curvature of y is proportional to θ. A perfectly tracked 1 V sine at 1 rad/s then gives a steady angular amplitude of about 0.243° if $K_x$=24 V/m. This result is independent of L for the chosen output. Large angle peaks around reference changes arise from transients and can have strong length dependence even when the periodic outputs coincide.

$$\begin{aligned} \ddot{y} &= K_x g\theta, \\ \frac{\Theta(j\omega)}{Y(j\omega)} &= -\frac{\omega^2}{K_x g} \\ |\theta_{ss}| &= \frac{1}{24(9.81)} \\ &\simeq 0.00425 \text{ rad} \quad (a = 1 \text{ V}) \end{aligned} \tag{3.19}$$

**Table 3.1** – Unstable pole magnitude and ratio of nominal cart frequency to pendulum rate.

| L (m) | λ ($s^{-2}$) | α ($s^{-1}$) | $\omega_c/\alpha$ |
|---|---|---|---|
| 0.16 | 61.312 | 7.830 | 6.60 |
| 0.23 | 42.652 | 6.531 | 7.91 |
| 0.28 | 35.036 | 5.919 | 8.73 |
| 0.35 | 28.029 | 5.294 | 9.76 |

## 3.7 Frequency range of the servo approximation

The ratios in Table 3.1 compare a cart frequency with the positive pendulum pole. They do not directly bound the frequency of the outer feedback crossover. Write $\rho=\omega/\omega_c$. The exact cart denominator on the imaginary axis is $1-\rho^2+j\,2\zeta\rho$. Replacing the transfer by its static gain one neglects a first-order phase lag even when its magnitude is close to one.

$$\begin{aligned} |H_1(j\omega)| &= \frac{1}{\sqrt{(1-\rho^2)^2 + 4\zeta^2\rho^2}} \\ \arg H_1(j\omega) &= -\arg(1 - \rho^2 + j2\zeta\rho) \end{aligned} \tag{3.20}$$

$$\begin{aligned} H_1(j\omega) &= 1 - j2\zeta\rho + O(\rho^2) \\ |H_1(j\omega) - 1| &= \frac{\sqrt{\rho^4 + 4\zeta^2\rho^2}}{\sqrt{(1-\rho^2)^2 + 4\zeta^2\rho^2}} \end{aligned} \tag{3.21}$$

At the reference frequency the nominal servo contributes about −1.10° of phase. At the retuned nominal crossover of the retained model it contributes about −9.86°, and at the shortest-length crossover about −23.7°. The adequacy of replacing $H_1$ by unity must therefore be judged relative to the question being asked. Accurate low-frequency tracking and a large discrepancy in the reported phase reserve can occur together.

# 4 Continuous-time controller synthesis

## 4.1 Nominal design assumptions

The target plant is $H_2$=B/A at $L_0$=0.35 m. At g=9.81 m/s$^2$, $\lambda_0$=28.0285714 s$^{-2}$ and $\alpha_0$=5.29420168 s$^{-1}$. Using the positive pole magnitude of the longest pendulum makes this the initial design point. The same numerical coefficients will subsequently be evaluated at shorter lengths. From equation (2.8), n = 2 and the choice δ = 0 give degree four in R and S and degree six in the closed-loop characteristic polynomial.

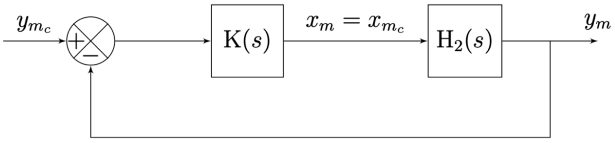


**Figure 4.1** – Original reduced-design loop [1, PDF p. 17]. The inner position servo is replaced by unit static gain for synthesis. Original Fig. 4.1.

$$A_0 = s^2 - \lambda_0, \quad B_0 = -\lambda_0$$
$$S = s(s^2 + \omega_0^2)(s + c_1) \tag{4.1}$$
$$R = r_0 s^4 + r_1 s^3 + r_2 s^2 + r_3 s + r_4$$

The shared denominator S incorporates the three required forcing frequencies. The remaining first-order factor adjusts the coefficient of $s^5$ in AS. The equal degree allows a direct command term in the controller, which is realised with four dynamic states and a finite feedthrough. A continuous plant output still produces a discontinuous demand when the reference or sensor input changes abruptly.

## 4.2 Choice and expansion of the pole product

The archive places a real pole and a conjugate pair at real part −β, keeps a pair at $-\alpha_0$ and sets the sixth pole to −γ. The target repeats $-\alpha_0$ to avoid keeping the unstable open-loop pole. The phrase “keeps a pair” describes the pole allocation, not a cancellation of a mode in the feedback path. The closed-loop pair is repeated on the nominal reduced model only. The parameter β sets the designated speed of the slow group and γ places the extra fast pole. With the servo retained, the target product no longer equals the characteristic polynomial.

$$\mathcal{P}_\star = \{-\gamma, -\alpha_0, -\alpha_0, -\beta, -\beta \pm j\omega_0\}$$
$$P_\star = (s+\gamma)(s+\alpha_0)^2 \times (s+\beta)[(s+\beta)^2 + \omega_0^2] \tag{4.2}$$

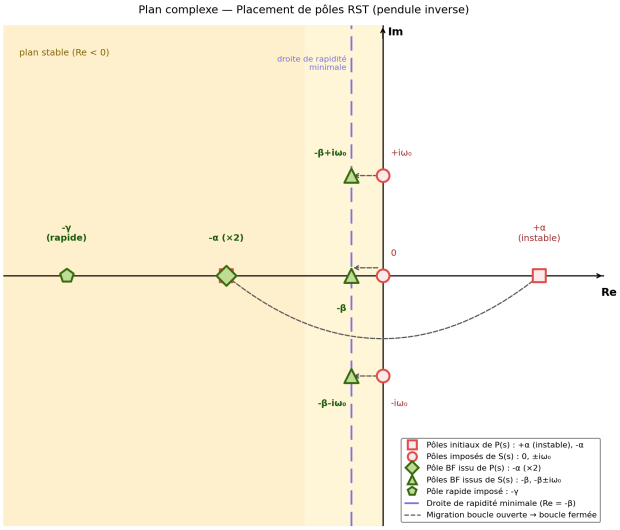


**Figure 4.2** – Source complex-plane construction [1, PDF p. 18]. The right-half-plane open-loop pendulum pole is displaced in the desired configuration. The upright and internal-model modes are visible in the original sketch. Original Fig. 4.2.

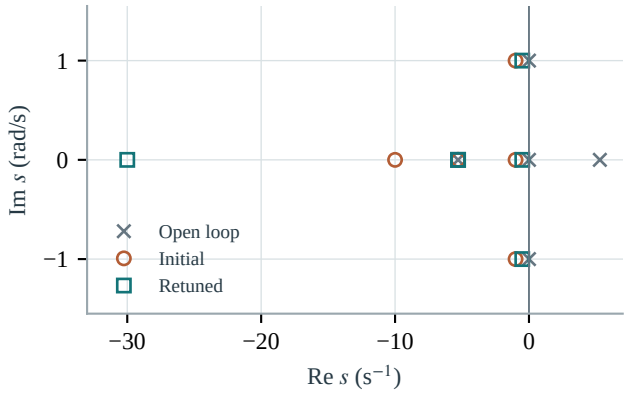


**Figure 4.3** – Recomputed poles of the nominal reduced model for the two pole allocations. The nonzero imaginary-axis markers are open-loop internal-model poles. A double target real pole appears as coincident markers.

To compute the coefficients without repeated root multiplication, write the real-pole factor $(s+\gamma)(s+\alpha_0)^2=s^3+a_1s^2+a_2s+a_3$. The internal-model-related group similarly has coefficients $b_1,b_2,b_3$. This separates the dependence on $(\alpha_0,\gamma)$ from that on $(\beta,\omega_0)$.

$$\begin{aligned} a_1 &= 2\alpha_0+\gamma, \quad a_2 = \alpha_0^2+2\alpha_0\gamma \\ a_3 &= \alpha_0^2\gamma \\ b_1 &= 3\beta, \quad b_2 = 3\beta^2+\omega_0^2 \\ b_3 &= \beta(\beta^2+\omega_0^2) \end{aligned} \tag{4.3}$$

Each coefficient is a convolution of the two four-term vectors. The leading coefficient is one. Matching $P_\star=s^6+c_1s^5+c_2s^4+c_3s^3+c_4s^2+c_5s+c_6$ then gives six scalar identities.

$$\begin{aligned} c_1 &= a_1+b_1, \quad c_2 = a_2+a_1b_1+b_2 \\ c_3 &= a_3+a_2b_1+a_1b_2+b_3 \\ c_4 &= a_3b_1+a_2b_2+a_1b_3 \\ c_5 &= a_3b_2+a_2b_3, \quad c_6 = a_3b_3 \end{aligned} \tag{4.4}$$

**Table 4.1** – Monic target coefficients below degree six.

| Term | Initial | Retuned |
|---|---|---|
| $c_1$ | 23.5884 | 42.0884 |
| $c_2$ | 199.6778 | 408.3133 |
| $c_3$ | 766.3771 | 1431.0329 |
| $c_4$ | 1417.6844 | 1891.5946 |
| $c_5$ | 1388.9681 | 1687.5504 |
| $c_6$ | 560.5714 | 525.5357 |

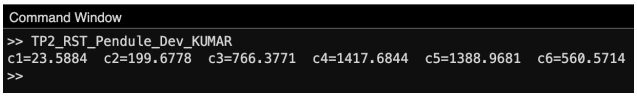


**Figure 4.4** – Archived initial target coefficients [1, PDF p. 19]. The values can be compared with the initial column of Table 4.1. Original Fig. 4.3.

The two sets of $c_1$ through $c_6$ have substantially different middle coefficients. For instance the retuned $c_2$ is about 408.31, above the initial 199.68, mainly as a result of pushing the extra pole from −10 to −30. The retuned $c_6$ is smaller because it is proportional to $\gamma\beta(\beta^2+\omega_0^2)$. The coefficient changes are therefore not equivalent to scaling the entire controller by a constant. The slower dominant target rate and faster auxiliary pole are independent design choices.

## 4.3 Matching the Bézout coefficients

Multiplying S by $A_0$ gives fixed terms in powers from six down to one. Subtracting this product from $P_\star$ determines the feedback polynomial after division by $B_0=-\lambda_0$. Because R has degree at most four, the $s^5$ coefficient of $A_0$ S must equal $c_1$. Collecting each remaining power yields equation (4.6).

$$\begin{aligned} A_0S &= s^6+c_1s^5+(\omega_0^2-\lambda_0)s^4 \\ &\quad +c_1(\omega_0^2-\lambda_0)s^3 \\ &\quad -\lambda_0\omega_0^2s^2-\lambda_0c_1\omega_0^2s \\ R &= \frac{P_\star-A_0S}{-\lambda_0} \end{aligned} \tag{4.5}$$

$$\begin{aligned} r_0 &= \frac{\omega_0^2-\lambda_0-c_2}{\lambda_0} \\ r_1 &= \frac{c_1(\omega_0^2-\lambda_0)-c_3}{\lambda_0} \\ r_2 &= -\omega_0^2-\frac{c_4}{\lambda_0} \\ r_3 &= -c_1\omega_0^2-\frac{c_5}{\lambda_0} \\ r_4 &= -\frac{c_6}{\lambda_0} \end{aligned} \tag{4.6}$$

As a numerical check for the initial design, $r_2=-1-1417.68437/28.02857=-51.579972$. The source's archived MATLAB printout and its listing have the negative sign. The narrative coefficient line in [1, PDF p. 19] reports +51.58. Inserting that

positive value into R would make the coefficient of $s^2$ in P about −1474 instead of +1418. A real monic Hurwitz polynomial is a product of positive-coefficient linear factors and stable real quadratic factors, so it cannot have a negative coefficient. This provides an independent way to detect the transcription error.

```
Command Window
Sigma1=23.5884
r0=-8.0884  r1=-50.0895  r2=-51.5800  r3=-73.1438  r4=-20.0000
>>
```

**Figure 4.5** – Archived initial Bézout coefficient solution [1, PDF p. 19]. The negative printed value of $r_2$ agrees with equation (4.6). Original Fig. 4.4.

The report and accompanying script evaluate the complete closed-loop polynomial residual before rounding. The nominal six coefficients are not estimates obtained by fitting a time trajectory. They follow uniquely from the chosen pole set, the internal model and $B_0$. Appendix A lists R and S, together with the full T coefficients.

## 4.4 Feedforward interpolation

Set F(s)=(s+γ)(s+β) and define $Q_T=q_0s^2+q_1s+q_2$, so $T=FQ_T$. At the nominal design this F removes two real target factors from the reference transfer $B_0T/P_\star$. The corresponding factors are still present internally and appear in disturbance analyses. Away from the design plant, these cancellations generally do not persist.

$$\begin{aligned} T(s) &= (s+\gamma)(s+\beta)(q_0s^2+q_1s+q_2) \\ q_2 &= \frac{R(0)}{\gamma\beta} \\ \frac{Y}{R_f}\Big|_{H_2,L_0} &= \frac{B_0Q_T}{(s+\alpha_0)^2[(s+\beta)^2+\omega_0^2]} \end{aligned} \tag{4.7}$$

To solve the remaining two real equations at $j\omega_0$, write $F(j\omega_0)=a+jb$. Its real part is $a=\gamma\beta-\omega_0^2$ and its imaginary part is $b=\omega_0(\gamma+\beta)$. Also write $R(j\omega_0)=R_e+jR_i$. Substitution gives the equations for $q_0$,$q_1$ with $q_2$ already known.

$$\begin{aligned} R_e &= r_0\omega_0^4 - r_2\omega_0^2 + r_4 \\ R_i &= -r_1\omega_0^3 + r_3\omega_0 \\ -a\omega_0^2q_0 - b\omega_0q_1 &= R_e - aq_2 \\ -b\omega_0^2q_0 + a\omega_0q_1 &= R_i - bq_2 \end{aligned} \tag{4.8}$$

The determinant of this two-by-two system is $-\omega_0^3(a^2+b^2)$, nonzero for positive $\omega_0$, β and γ. For the initial design the real matrix rows are (−9,−11) and (−11,9). With the reconstructed R, the right-hand side is approximately (41.4916,−1.0543). Solving gives $q_0=-1.79122$, $q_1=-2.30642$ and $q_2=-2$. The retuned values are different because both the feedback and the real factors F change. Here $q_i$ names the quadratic coefficients, which the original console calls $t_i$.

$$\begin{aligned} v &= \frac{R(j\omega_0)}{F(j\omega_0)} \\ q_0 &= \frac{q_2 - \operatorname{Re} v}{\omega_0^2}, \\ q_1 &= \frac{\operatorname{Im} v}{\omega_0} \end{aligned} \tag{4.9}$$

**Table 4.2** – Quadratic interpolation coefficients inside F(s).

| Term | Initial | Retuned |
|---|---|---|
| $q_0$ | −1.79122 | −1.38669 |
| $q_1$ | −2.30642 | −1.05877 |
| $q_2$ | −2.00000 | −1.25000 |

```
Command Window
t0=-1.7912  t1=-2.3064  t2=-2.0000
>>
```

**Figure 4.6** – Archived $t_0$, $t_1$ and $t_2$ for the initial tuning [1, PDF p. 20]. The displayed numbers correspond to $q_0$, $q_1$ and $q_2$ in Table 4.2. Original Fig. 4.5.

Matching T and R at three points implies that their difference is divisible by the same internal-model factor used in S. Because both polynomials have degree four, $T-R=F_i\,Q_e$ for a polynomial of degree at most one. Consequently, the reference error numerator has the invariant factor $F_i$ as long as the controller and reference interpolation are held fixed. The remaining factor determines the size and slope of the error near those exact zeros.

$$T - R = F_i Q_e,$$
$$\frac{E}{R_f} = \frac{F_i(BQ_e - AQ)}{P} \tag{4.10}$$

This factorization will be used to read the detuning curves in Section 8. It also explains why the original reduced phase margin can change when the servo is included without changing the zero-error frequency, provided the augmented closed loop is stable.

# 5 Frequency-domain verification

## 5.1 Definitions and asymptotes

For the remainder of the frequency analysis use D=AS, N=BR and P=D+N. The return ratio L=N/D is defined using the subtraction in equation (2.3). The characteristic roots of the physical feedback interconnection are computed from P before any stable factors are cancelled in plotted transfer functions. For example, $A_0(-\alpha_0)=0$ and $R(-\alpha_0)=0$ in the nominal design. A reduced return-ratio display can hide a stable factor without removing that mode from the target characteristic polynomial.

$$\begin{aligned} \mathcal{L}(s) &= \frac{BR}{AS}, \\ 1+\mathcal{L} &= \frac{P}{D} \\ \mathcal{S} &= \frac{D}{P}, \\ \mathcal{T}_c &= \frac{N}{P} \end{aligned} \tag{5.1}$$

Here S is the closed-loop sensitivity and $T_c$ the complementary sensitivity [4]. The symbol S without calligraphic style denotes the controller denominator. For both models the integrator makes the low-frequency magnitude fall approximately 20 dB per decade as frequency increases. The coefficient of that asymptote is fixed by $r_4$ and the s coefficient of S. At the internal-model frequency the open-loop controller has a simple pole. The large peak in the archived Bode magnitude is a numerical rendering of this singularity. The stable closed-loop sensitivity tends to zero at the same point.

$$\begin{aligned} \mathcal{L}(s) &= \frac{r_4}{c_1\omega_0^2 s} + O(1) \\ &\quad (s \to 0) \\ \mathcal{L}(s) &= \\ &\frac{N(j\omega_0)}{D'(j\omega_0)(s-j\omega_0)} \\ &+ O(1) \quad (s \to j\omega_0) \end{aligned} \tag{5.2}$$

With the reduced plant and nonzero leading $r_0$, the high-frequency relative degree of the loop is two. The retained servo adds two, producing an asymptotic slope of −80 dB/decade compared with −40 dB/decade for the reduced model. The associated phase lag begins affecting the crossover well before the asymptote is fully established. In Figures 5.1 and 5.2 the two branches on either side of $\omega_0$ are drawn separately. A phase line through the open-loop pole would depend on the continuation convention.

$$\begin{aligned} \mathcal{L}_2(s) &\sim \frac{-\lambda r_0}{s^2} \\ \mathcal{L}_4(s) &\sim \frac{-\lambda r_0 \omega_c^2}{s^4} \end{aligned} \tag{5.3}$$

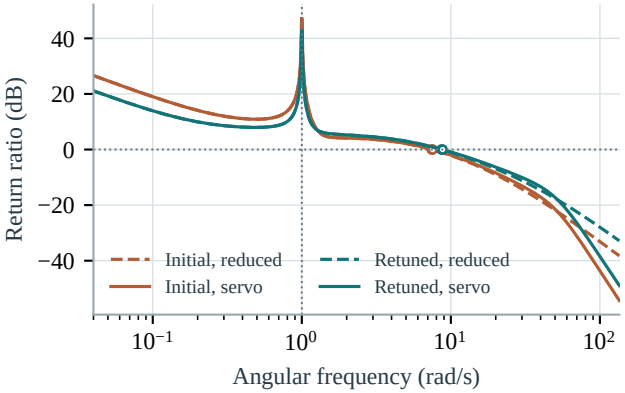


**Figure 5.1** – Nominal return-ratio magnitude for both controllers and both plants. Open circles mark gain crossovers. The gap at $\omega_0$ = 1 rad/s separates branches of the open-loop pole.

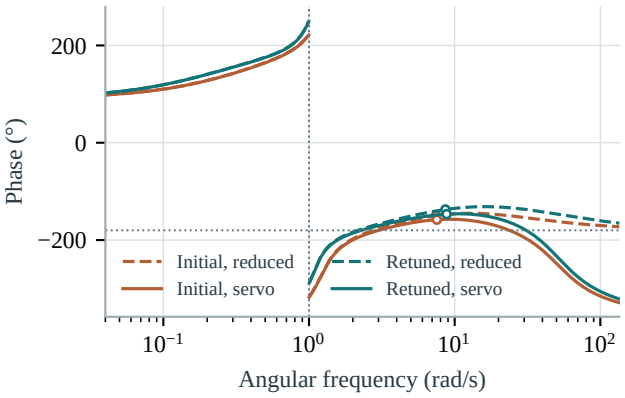


**Figure 5.2** – Nominal phase on the same branches. The post-resonance branch is shown modulo 360° with each unity-gain crossing aligned to its reported phase margin.

## 5.2 Reading the original Bode curves

The original initial-design plot shows a unity-gain crossing near 7.44 rad/s and phase margin near 30°. The MATLAB console gives 30.0289°, −3.8158 dB for the gain-margin crossing and a reported modulus margin of 0.4946. The algebraic result below recovers its crossovers and gives 0.4939 for the continuous-frequency modulus margin. The original sampled Nyquist calculation in [1, Appendix A] is a plausible source of the small modulus-margin difference. Independent comparison with the polynomial stationary-point check quantifies the error of the current calculation.

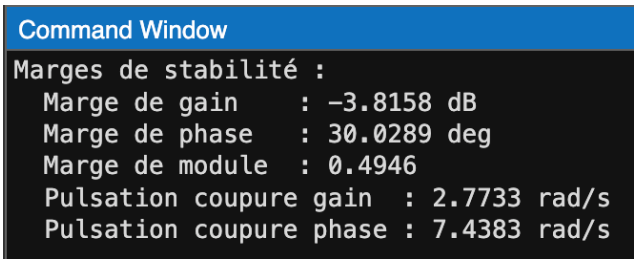


**Figure 5.3** – Archived initial margin annotations [1, PDF p. 21]. At 7.4383 rad/s the margin is 30.0289°. The negative gain-margin reading refers to a lower gain boundary. Original Fig. 5.1.

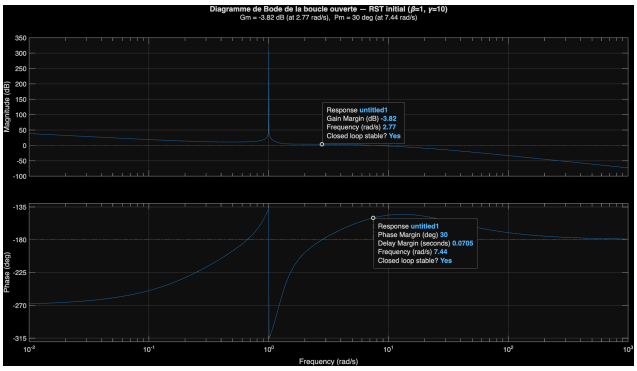


**Figure 5.4** – Archived initial Bode plot [1, PDF p. 22]. The dominant spike and phase discontinuity occur at the internal-model frequency. The unity-gain crossing is separate from the −180° crossing. Original Fig. 5.2.

The retuned original curve moves the unity-gain crossing to about 8.64 rad/s and raises the reduced-model phase margin to 42.8°. The reproduced Bode curves show the same trend with the servo included, but at lower margins. At nominal length the initial and retuned retained models give 21.9° and 33.3°, respectively. The retuning improves that model by 11.4° and falls short of the 40° target stated for the reduced design. At nominal length the change reflects both the extra phase and a modest crossover shift, so subtracting only the cart phase at the reduced model's crossover is an approximation.

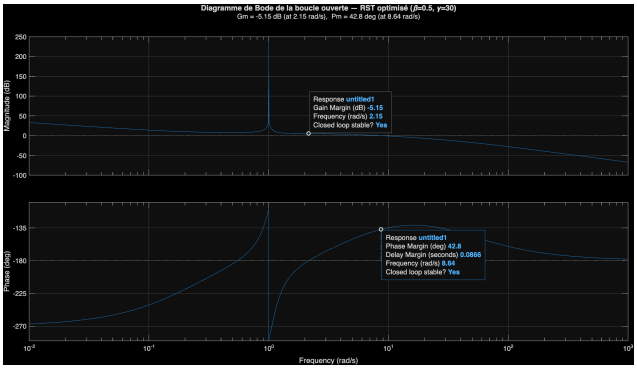


**Figure 5.5** – Archived retuned Bode plot [1, PDF p. 26]. The displayed margin of 42.8° corresponds to the reduced plant with β = 0.5 and γ = 30. Original Fig. 6.1.

**Table 5.1** – Nominal frequency response and return-distance margins.

| Tuning | Plant | $\omega_g$ (rad/s) | $\varphi_m$ (°) | $M_m$ |
|---|---|---|---|---|
| Initial | $H_2$ only | 7.44 | 30.03 | 0.494 |
| Initial | $H_1H_2$ | 7.55 | 21.87 | 0.379 |
| Retuned | $H_2$ only | 8.64 | 42.84 | 0.727 |
| Retuned | $H_1H_2$ | 8.80 | 33.32 | 0.557 |

## 5.3 Algebraic crossovers and stable gain intervals

For a real polynomial $p(s)=\sum a_k s^k$, substituting $s=j\sqrt{(z)}$ with $z=\omega^2$ separates its even and odd powers. This avoids grid interpolation at a narrow phase crossing. The real part contains the alternating even coefficients and the imaginary part contains the alternating odd coefficients times $\sqrt{(z)}$. The roots used below are positive real values of z, filtered by the intended complex equation.

$$\begin{aligned} p(j\sqrt{z}) &= p_e(z) + j\sqrt{z}\,p_o(z) \\ p_e(z) &= \sum_{i\geq 0} (-1)^i a_{2i} z^i \\ p_o(z) &= \sum_{i\geq 0} (-1)^i a_{2i+1} z^i \end{aligned} \tag{5.4}$$

At a unity-gain frequency $|N|^2=|D|^2$. A valid positive solution must have $D(j\omega)\neq 0$. At a crossing

for scalar positive feedback gain multiplier k, the characteristic polynomial satisfies D+kN=0. The reality condition for D/N and positivity of k give a second equation. Singular points are excluded from that calculation as well.

$$\begin{aligned} N_e^2 + zN_o^2 - D_e^2 - zD_o^2 &= 0 \\ k = -\frac{D(j\omega)}{N(j\omega)} &> 0 \\ D_oN_e - D_eN_o &= 0 \end{aligned} \tag{5.5}$$

The leading coefficient of D+kN is constant in k. Since D(0)=0 and N(0)≠0, a zero root is possible only at k = 0. Along the positive gain axis a change in the root count must otherwise pass through a nonzero imaginary pair. The connected interval about k = 1 is found by locating the closest positive crossings and checking stability at the nominal gain. At the initial reduced design there is a lower boundary near 0.64448, equivalent to 20 $\log_{10}(0.64448)$ = −3.8158 dB. The archive's negative number therefore denotes a gain reduction from the nominal value. At about 2.773 rad/s the corresponding real Nyquist coordinate is −1/0.64448≃−1.552. The retained servo narrows the gain range on both ends for the two tunings compared here.

**Table 5.2** – Connected gain interval about k = 1 and pure-delay threshold at nominal length.

| Tuning | Plant | Gain interval | τ (ms) |
|---|---|---|---|
| Initial | $H_2$ only | (0.644, ∞) | 70.5 |
| Initial | $H_1H_2$ | (0.653, 3.278) | 50.6 |
| Retuned | $H_2$ only | (0.553, ∞) | 86.6 |
| Retuned | $H_1H_2$ | (0.558, 3.295) | 66.1 |

## 5.4 Generalized Nyquist count

Open-loop unstable and marginal poles require a contour choice. The pendulum contributes one strictly right-half-plane pole +α; the internal model contributes the axis poles at 0 and ±j$\omega_0$. The physical frequency curve alone leaves its continuation around those poles unspecified. To test the count, let F=1+L=P/D and use a positively oriented right half-disc offset to Res=ε>0. The boundary goes down the vertical edge and back up the right semicircle. With this orientation the winding of F around zero equals the number of enclosed zeros minus the number of enclosed poles.

$$\begin{aligned} W_F &= \frac{1}{2\pi}\Delta_{\Gamma_\varepsilon}\arg F \\ &= Z_P - P_D \end{aligned} \tag{5.6}$$

The offset excludes the axis poles and retains the unstable pendulum pole. For all compared end-length cases, the closed-loop roots give $Z_P$=0, and the denominator gives $P_D$=1. Thus $W_F$=−1 for the stated orientation. Reversing the contour reverses the sign. The common description of a counter-clockwise encirclement of −1 uses the opposite contour orientation for the right half-plane. Stating the sign convention makes the two descriptions compatible.

The computation also sums arg($F_{i+1}/F_i$) along the sampled offset contour. Three choices of positive offset and radius are applied to the two tunings, two plants and two endpoint lengths. All 24 runs give −1. The maximum neighbouring argument change is about 0.049 rad on those grids, and the count agrees with the characteristic roots. This complements the archived frequency-only images because the summation includes the continuation near the excluded axis poles and the closing arc.

$$\begin{aligned} \widehat{W}_F &= \frac{1}{2\pi}\sum_{i=0}^{M-1} \\ &\arg\frac{F(s_{i+1})}{F(s_i)}, \quad s_M = s_0 \end{aligned} \tag{5.7}$$

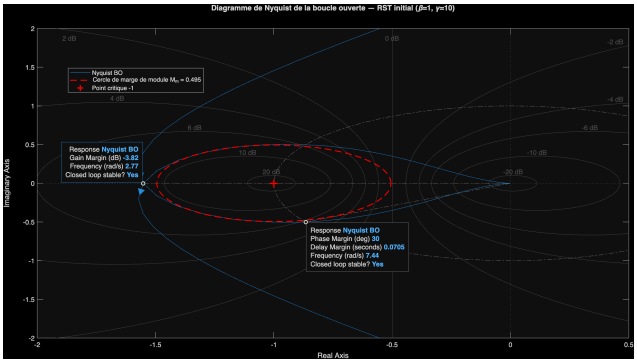


**Figure 5.6** – Initial-design Nyquist image from [1, PDF p. 22]. The arc close to −1 motivates the modulus margin. Its visible window does not show the full Nyquist contour. Original Fig. 5.3.

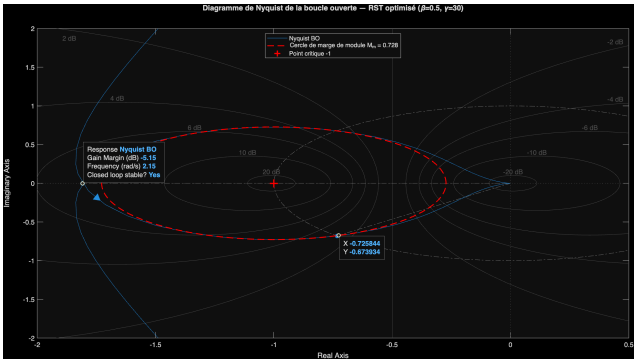


**Figure 5.7** – Retuned Nyquist image from [1, PDF p. 26]. The minimum distance to −1 is larger than in the initial reduced case. The enlarged distance supports the reduced-model margin comparison. Original Fig. 6.2.

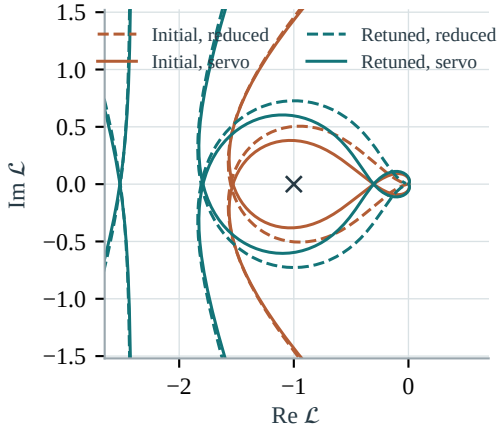


**Figure 5.8** – Recomputed frequency loci near the critical point at nominal length. The branches reflect positive and negative frequencies. The complete oriented count is evaluated by equation (5.7).

The retained and reduced loops have the same count for these cases, but the nearest approach to the critical point changes. The nominal retuned trace with the servo runs closer to −1 than its reduced counterpart. This explains why preserving the nominal winding does not preserve robust stability margins. The source's Nyquist plots support local geometric comparisons of their respective models.

## 5.5 Modulus margin and peak sensitivity

The modulus margin $M_m$ is the smallest distance between the Nyquist locus and the critical point, evaluated over frequency with limiting values where appropriate. It is the reciprocal of peak sensitivity $M_S$. This definition incorporates magnitude and phase simultaneously. A phase margin samples one circle crossing and does not determine the closest point of the curve.

$$\begin{aligned} M_m &= \inf_{\omega \geq 0} |1 + \mathcal{L}(j\omega)| \\ &= \frac{1}{M_s}, \\ M_s &= \sup_{\omega \geq 0} |S(j\omega)| \end{aligned} \tag{5.8}$$

The computation first refines local maxima of |D/P| on a logarithmic frequency grid. A second calculation eliminates the search-grid assumption. Write $Q_D(z)=D_e^2+zD_o^2$ and similarly $Q_P(z)$. At a stationary point of $Q_D/Q_P$ the numerator of its derivative is zero. Valid roots with z>0 and the limiting values at zero and infinity yield the candidate peaks. Agreement between the two methods is within $6\times10^{-11}$ in peak sensitivity for the 16 combinations of model, tuning and length.

$$\begin{aligned} |S(j\sqrt{z})|^2 &= \frac{Q_D(z)}{Q_P(z)} \\ Q_D' Q_P - Q_D Q_P' &= 0 \end{aligned} \tag{5.9}$$

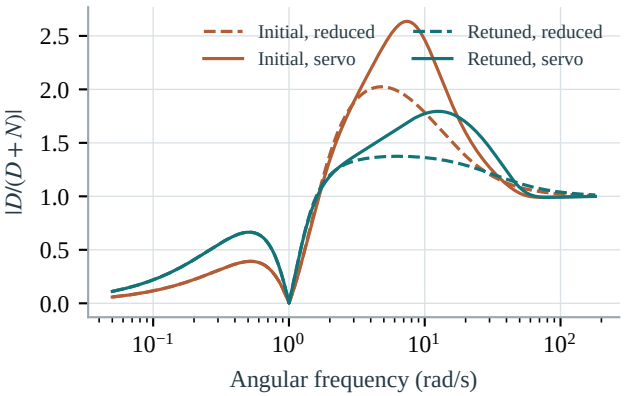


**Figure 5.9** – Nominal sensitivity magnitude. The notch at 1 rad/s comes from the zeros of S. The maxima in Table 5.3 determine the modulus margins.

**Table 5.3** – Peak output sensitivity at nominal length.

| Tuning | Plant | $M_S$ | ω at peak (rad/s) |
|---|---|---|---|
| Initial | $H_2$ only | 2.025 | 4.80 |
| Initial | $H_1H_2$ | 2.637 | 7.39 |
| Retuned | $H_2$ only | 1.375 | 6.33 |
| Retuned | $H_1H_2$ | 1.795 | 12.58 |

The retuned reduced design increases $M_m$ from about 0.494 to 0.727. With the cart poles retained

the corresponding comparison is 0.379 to 0.557. In the nominal retained model the retuning lowers the maximum sensitivity, but its high-frequency conversion of sensor perturbations into demand increases. Equation (2.4) gives $U/N_b=-AR/P$. Since $P\sim AS$ at high frequency, its magnitude tends to $|r_0|$. Figure 5.10 shows how this limit differs between tunings even though S tends to one.

$$\begin{aligned} \frac{U}{N_b} &= -\frac{AR}{P} \\ &= -\frac{R}{S}\mathcal{S} \\ \lim_{\omega\to\infty}\left|\frac{U}{N_b}\right| &= |r_0| \end{aligned} \tag{5.10}$$

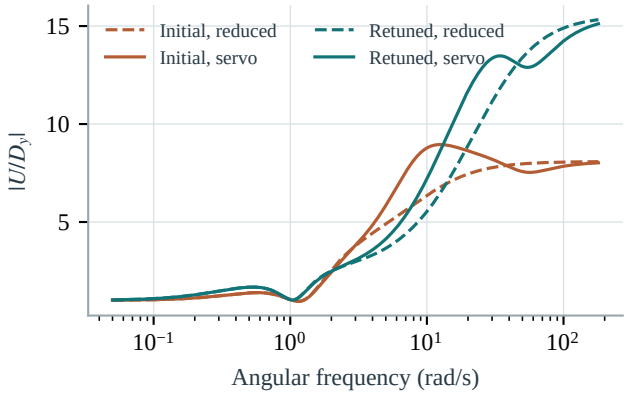


**Figure 5.10** – Magnitude from sensor corruption to outer command. The retained servo changes the intermediate-frequency shape. The large-frequency limits are set by the feedback leading coefficients.

## 5.6 An additional transport-delay threshold

For fixed plant and controller a pure delay multiplying the return ratio leaves its magnitude unchanged. A root on the imaginary axis first requires some $\omega_g$ with unit return-ratio magnitude. Each tested loop in Table 5.2 has one such frequency on a decreasing curve. Defining phase margin in radians by the smallest positive phase lag to the negative real axis gives equation (5.11). A zero-frequency crossing is ruled out by the nonzero characteristic value at s = 0 and the delay is in a retarded characteristic equation of strictly proper loop order.

$$\begin{aligned} \phi_m &= (\arg \mathcal{L}(j\omega_g) + \pi) \bmod 2\pi \\ \tau_{\text{crit}} &= \frac{\phi_m}{\omega_g} \end{aligned} \tag{5.11}$$

The sign of root motion can be checked by differentiating $1+L(s)e^{-s\tau}=0$ with respect to $\tau$. At $s=j\omega_g$, a decreasing magnitude implies that the imaginary part of $L'/L$ is positive, because it is the negative of the derivative of $\ln|L(j\omega)|$. Multiplication by the conjugate denominator then gives a positive real part of $ds/d\tau$. The crossing therefore moves into the right half-plane as the delay increases locally through its first boundary.

$$\begin{aligned} \frac{ds}{d\tau} &= \frac{s}{\mathcal{L}'(s)/\mathcal{L}(s) - \tau} \\ \frac{d\ln|\mathcal{L}(j\omega)|}{d\omega} &= -\operatorname{Im}\frac{\mathcal{L}'(j\omega)}{\mathcal{L}(j\omega)} \end{aligned} \tag{5.12}$$

For the retuned nominal plant the predicted threshold changes from 86.6 ms to 66.1 ms when the cart is retained. This is a model-specific additional pure-delay threshold. A sampled implementation also has hold, discretisation and computational dynamics. Those effects need their own model.

# 6 Reading the archived Simulink curves

## 6.1 Signal routing and command sequence

The Simulink schematic is useful for attributing changes to the correct signal. A sinusoidal branch and a separate step branch add before the tap marked *ymc*. A second additive block, marked Group 1, is placed after the combination of cart and angular signals and before the tap marked *ym*. Under the notation of Section 2, *ymc* is r and *ym* is z. The signal u is tapped before the plant block labelled *num(s)/den(s)*. Those taps clarify which traces can be compared as output, measurement and command.

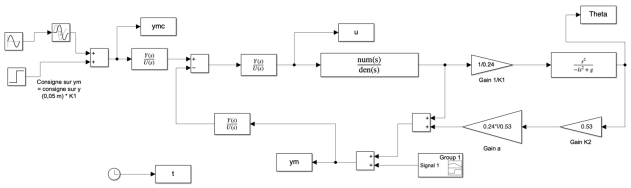


**Figure 6.1** – Original Simulink implementation [1, PDF p. 23]. The reference sum is at left. Group 1 adds near the measured output at the bottom. The cart-servo numerator and denominator are not expanded in the image. Original Fig. 5.4.

The graph begins with a quiet interval, followed by a preparation transient near 3.25–3.33 s, a sinusoidal reference from about 5 s and an offset shift at 15 s. The schematic supports the existence of both a reference step and an additive measurement signal. The exact timing, amplitude and shape of Group 1, and the initial state or forcing responsible for the earlier transient, cannot be read from the PDF. The labels around the sensor gains document the scaling structure. The raw values entering each block during the recorded run remain unspecified.

The reference component used in Python is a unit sine starting at 5 s plus a unit step at 15 s. This choice gives sin(10)=−0.544021 V just before the step, a useful check against the cursor on the initial close-up. After the step it gives 1+sin(t−5). The following comparison uses the graphical cursor coordinates as observations of those traces. When two curves overlap, the cursor label alone is insufficient to identify which channel is selected.

## 6.2 Initial tuning

The original wide-window record has four panels. The top panel shows that the measured output and reference are close through most of the periodic tracking interval. The second panel exposes brief errors of opposite sign around preparation and reference changes. At approximately 15 s the reference shifts abruptly and the measured output evolves continuously at plotting resolution. The command stays within the visibly marked ±5 V band. The last panel shows that the angular motion is concentrated around the transient times, with a markedly smaller oscillation between them.

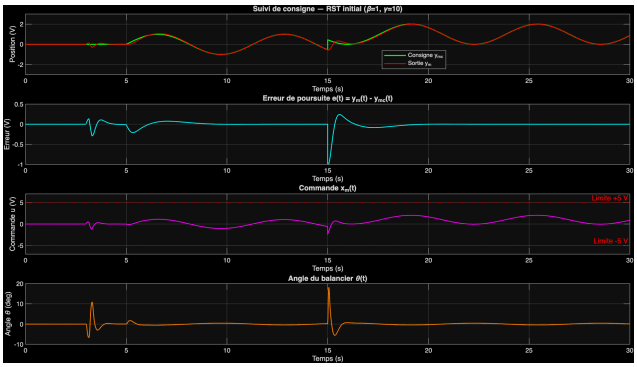


**Figure 6.2** – Initial Simulink time record [1, PDF p. 23]. From top to bottom: reference and measured position, tracking error, outer command and pendulum angle. Original Fig. 5.5.

The time close-up in Figure 6.3 shows the green reference stepping from approximately −0.54 V to +0.46 V, while the red trace first stays near its original level and then rises. A later marker is at 16.35 s and 0.0655384 V. The reconstructed reference would be about 0.06215 V at that time. The marker is near an intersection, consistent with a first visible re-approach of the curves. It does not specify that the error remains inside any given band afterwards.




**Figure 6.3** – Initial tuning around the 15 s change [1, PDF p. 24]. Data cursors are at (15 s, −0.543993 V) and (16.35 s, 0.0655384 V). Green is the reference. Original Fig. 5.6.

The two annotated angle peaks are 10.033° at 3.33 s and 17.5613° at 15.05 s. The rapid post-step positive excursion in Figure 6.4 is followed by a negative lobe. The small oscillation in the subsequent tracking interval is compatible with a small steady-state angle and appreciable transient curvature of the combined position signal. The first-marked peak belongs to the preparation period and must not be attributed to the 15 s reference change.

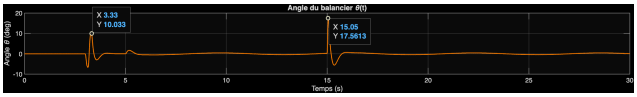


**Figure 6.4** – Initial angular record [1, PDF p. 24]. The later positive peak is 17.5613° at 15.05 s. Original Fig. 5.7.

## 6.3 Retuned trace and correction of an angle reading

The retuned record has the same plotted signals and the same visible reference structure. The sine is accurately followed over most of the plot, the output lags the reference offset change and the command remains inside the displayed bound. The step close-up places the later cursor at 16.55 s. Its ordinate, 0.149797 V, matches 1+sin(11.55) to the displayed precision. This agreement is evidence for the reconstructed reference, while the free response and any additive measurement sequence remain separate questions.

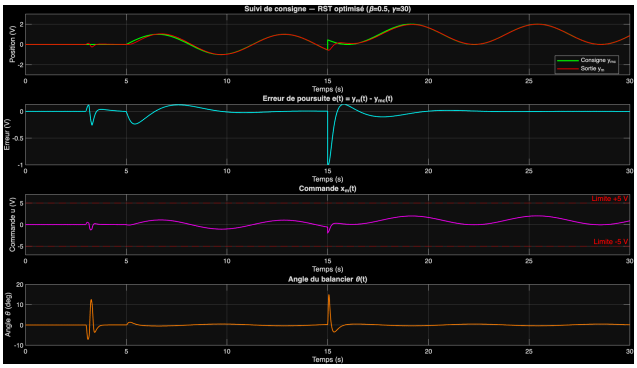


**Figure 6.5** – Retuned Simulink time record [1, PDF p. 27]. It shows reference and measurement, tracking error, outer command and angle over the same horizon as Figure 6.2. Original Fig. 6.3.

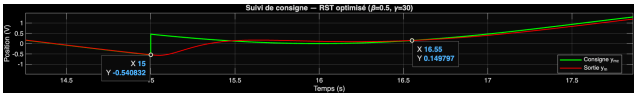


**Figure 6.6** – Retuned reference-step close-up [1, PDF p. 27]. The later marker is at (16.55 s, 0.149797 V). Original Fig. 6.4.

The angular close-up supplies a correction. At the later transient the plotted marker reads **X = 15.05 s** and **Y = 14.3023°**. The narrative in the original report uses 15.05° for the peak. That number is the time coordinate. Reading the two original plots at their marked peaks gives an angular reduction of approximately 18.6%. The early positive peak increases from 10.033° in the initial plot to 12.3637° in the retuned plot. Those early and late comparisons describe different events, and the retuning did not reduce both displayed angles.

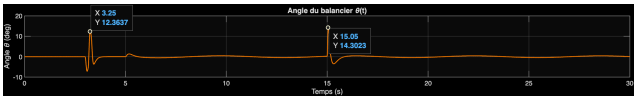


**Figure 6.7** – Retuned angular record [1, PDF p. 27]. The preparation peak is 12.3637° at 3.25 s. The later marker is 14.3023° at 15.05 s. Original Fig. 6.5.

**Table 6.1** – Visible annotations in the archived time histories. Time differences use the nominal 15 s edge.

| Tuning | Later cursor (s) | Δt (s) | Angle at peak (°) |
|---|---|---|---|
| Initial | 16.35 | 1.35 | 17.56 |
| Retuned | 16.55 | 1.55 | 14.30 |

$$\Delta_\theta = 1 - \frac{14.3023}{17.5613} \simeq 0.1856 \qquad t_{\text{cursor}} - 15 \in \{1.35,\ 1.55\}\ \text{s} \tag{6.1}$$

The 0.20 s difference is a comparison of graphical cursor intervals. A reproducible settling time for a sinusoid with changing mean needs an error definition and a band with a stated persistence criterion. A step in the reference tests the T branch. A physical disturbance enters a different transfer in equation (2.4). With both potentially present in the archive, assigning the full cursor interval to disturbance rejection would overstate what can be reconstructed.

## 6.4 Original four-length comparison

The MATLAB console for the retuned design reports phase margins of 48.4734°, 47.9730°, 46.1501° and 42.8365° for increasing length. They reproduce the recalculated reduced plant margins to rounding. The text assertion of a margin above 48° at every length is inconsistent with the console. The test uses one common set of controller polynomials, as can be checked in the original length loop. The instability claim that can be tested from these traces is local and model-specific.

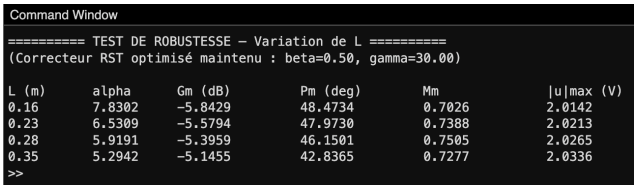


**Figure 6.8** – Archived four-length MATLAB comparison [1, PDF p. 28]. The numeric phase margins and command peaks are read directly from this panel. Original Fig. 7.1.

The four measured-position histories nearly coincide on the scale of the first panel, while the angular transients separate sharply. The original command maxima rise only from 2.0142 V at 0.16 m to 2.0336 V at 0.35 m, a spread of about 0.0194 V. Similar command peaks therefore give little information about the relative angle peaks or the reduction in the reserve to a high-frequency perturbation.

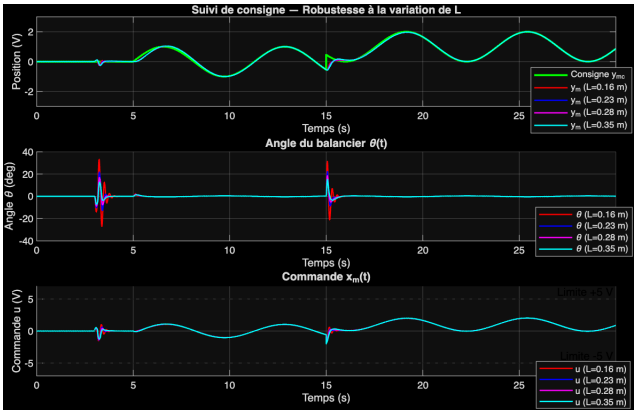


**Figure 6.9** – Original four-length time histories [1, PDF p. 29]. The combined outputs and commands nearly coincide. The middle trace group is the pendulum angle. Original Fig. 7.2.

In the zoom, a marked ordinate near 0.154714 V occurs at 16.56 s, near the reconstructed reference of 0.15510 V. The red trajectory for the shortest pendulum visibly departs more from the group close to the step. Near the later cursor the trajectories are close relative to the axis scale. This supports a weak length effect in that particular measured-output plot. It cannot establish an almost invariant band return for different disturbance locations.

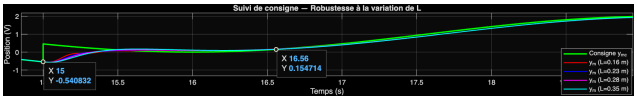


**Figure 6.10** – Original four-length zoom on the offset change [1, PDF p. 29]. The group approaches the moving reference after the step. Original Fig. 7.3.

The isolated angle plots expose two different peaks at short length: about 31.3258° at 3.25 s and 29.3755° at 15.07 s. The plotted short-length negative value of −21.1005° near 15.18 s is also larger in magnitude than the companion long-length curves at that point. The larger angle is not evidence of a larger steady-state sine error. It occurs during a higher-curvature transient. A small-angle check for these magnitudes is calculated in Section 9.

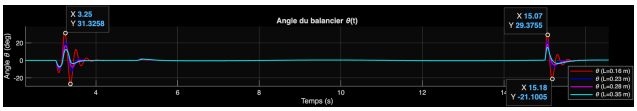


**Figure 6.11** – Original angle comparison by length [1, PDF p. 30]. The largest annotated calibration excursion is 31.3258°. The 15 s response includes both positive and negative lobes. Original Fig. 7.4.

# 7 Robustness to length, cart dynamics and retuning

## 7.1 Continuous length as a polynomial parameter

Changing L changes λ=g/L. The controller is held fixed, including its nominal factor $c_1$; recomputing the Bézout equation at each L would test a different controller. In the retained loop $A=D_c(s)(s^2-\lambda)$ and $B=-\lambda$. Expand P as an affine function of λ. The same expression covers the reduced plant by setting $D_c=1$.

$$\begin{aligned} P(s;\lambda) &= U_\lambda(s) - \lambda V_\lambda(s) \\ U_\lambda &= s^2 D_c S, \\ V_\lambda &= D_c S + R \end{aligned} \tag{7.1}$$

The subscripts in $U_\lambda, V_\lambda$ indicate this parameterization; neither polynomial contains λ. For a root on the positive imaginary axis the ratio $U_\lambda(j\omega)/V_\lambda(j\omega)$ must be real and positive. Using the even and odd decomposition of equation (5.4) gives a single polynomial condition in $z=\omega^2$. Multiplying the ratio by the conjugate denominator gives the real value of λ explicitly.

$$\begin{aligned} U_o V_e - U_e V_o &= 0, \qquad z > 0 \\ \lambda &= \\ \frac{U_e V_e + z U_o V_o}{V_e^2 + z V_o^2} &> 0 \\ L &= \frac{g}{\lambda} \end{aligned} \tag{7.2}$$

The case $V_\lambda(j\omega)=0$ would require $U_\lambda(j\omega)=0$. At the imaginary roots of $s^2 D_c S$, namely 0 and $\pm j\omega_0$, $V_\lambda=R\neq 0$. The origin is excluded separately by $P(0)=-\lambda R(0)\neq 0$ for $\lambda > 0$. The highest coefficient of P is independent of λ, so finite changes in L within the interval cannot cause a loss of degree. Coefficients depend continuously on L. Thus, starting from a stable nominal point, a change in the number of right-half-plane roots would need one of the crossings enumerated by equation (7.2).

The relevant parameter interval is $[9.81/0.35, 9.81/0.16]=[28.03, 61.31]\ s^{-2}$. The computed crossings lie outside it for both tunings and both plant orders. For the retained initial controller the nearest candidate lengths on the two sides are 0.09470 and 1.11473 m. For the retained retuned controller they are 0.09911 and 2.11662 m. These distances are quoted to describe the algebraic calculation; extension of the servo and mechanical models to those lengths would require its own justification. Inside 0.16–0.35 m, the root count from the nominal closed loop is preserved in the modeled continuous-length family.

## 7.2 Root motion and repeated poles

Length mismatch changes every coefficient of $-\lambda V_\lambda$. At a simple root, implicit differentiation gives the local derivative in equation (7.3). Near the repeated $-\alpha_0$ root of the nominal reduced pole product the simple-root derivative is singular. Expanding about this point gives a quadratic term in root displacement and a first-order term in parameter displacement. Unless the latter also vanishes, the two roots can split at order $\sqrt{(|\Delta\lambda|)}$. Moving only the originally doubled pole by the formula $-\sqrt{(g/L)}$ is therefore not the fixed-controller pole trajectory.

$$\begin{aligned} \frac{ds}{dL} &= -\frac{\lambda}{L} \\ \frac{V_\lambda(s)}{\partial P/\partial s} & \\ (\Delta s)^2 &\simeq \\ \frac{2V_\lambda(-\alpha_0)\Delta\lambda}{P_{ss}(-\alpha_0;\lambda_0)} & \end{aligned} \tag{7.3}$$

The retained retuned system has dominant poles near $-0.485 \pm j\,0.987$ at 0.35 m. At 0.16 m the corresponding poles are near $-0.478 \pm j\,1.006$. Meanwhile, at short length a faster pair near $-6.61 \pm j\,25.44$ is present. The small shift of the dominant pair explains the nearly constant largest real part without implying a nearly constant frequency reserve. Figures 7.1 and 7.2 make these distinct effects visible.

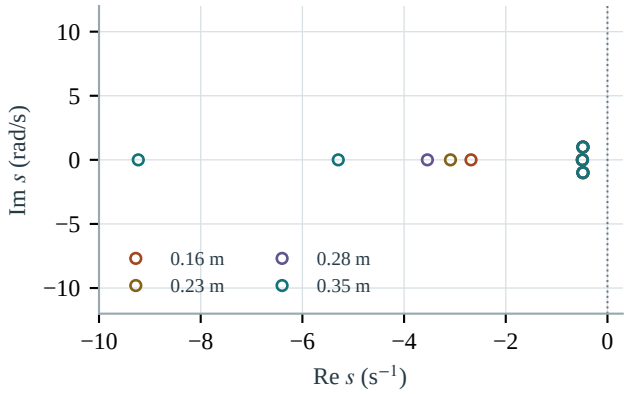


**Figure 7.1** – Selected poles of the fixed retuned RST and retained servo at four lengths. Fast modes beyond the plotted window are omitted from this figure and remain in the numerical characteristic polynomials.

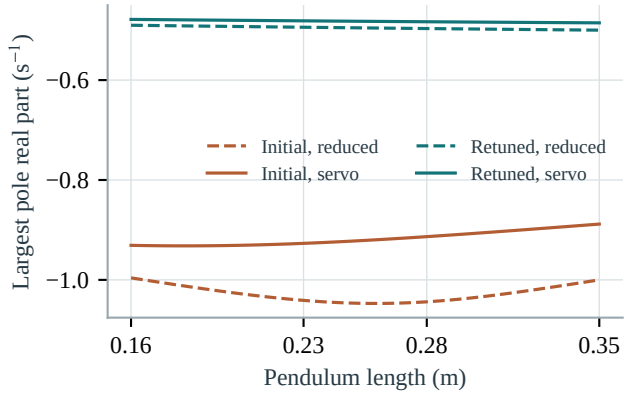


**Figure 7.2** – Largest real part of the characteristic roots through the length sweep. A nearly flat value describes long-tail decay in the tested linear models; the faster modes can still change markedly.

## 7.3 The length sweep is sensitive to plant order

The reduced-system phase margin of the retuned controller rises as L falls over the four archived lengths. The retained system has a smaller margin, especially at the shortest length. When the length is shortened from 0.35 to 0.16 m, its unity-gain crossover rises from 8.80 to 19.59 rad/s and the shortest-length servo phase there is approximately −23.7°. Both the increased phase lag and the higher crossover reduce the additional pure-delay threshold. Tables 7.1 and 7.2 compare the quantities at the same controller settings.

**Table 7.1** – Phase margin and additional pure-delay threshold for the fixed retuned RST.

| L (m) | $\varphi_m$, $H_2$ (°) | $\varphi_m$, $H_1H_2$ (°) | $\tau$, $H_1H_2$ (ms) |
|---|---|---|---|
| 0.16 | 48.47 | 24.44 | 21.8 |
| 0.23 | 47.97 | 32.70 | 42.3 |
| 0.28 | 46.15 | 34.01 | 53.9 |
| 0.35 | 42.84 | 33.32 | 66.1 |

**Table 7.2** – Return ratio and pole metrics for the same retuned RST with the cart servo.

| L (m) | $\omega_g$ (rad/s) | $M_m$ | $\sigma$ ($s^{-1}$) |
|---|---|---|---|
| 0.16 | 19.59 | 0.290 | −0.478 |
| 0.23 | 13.49 | 0.448 | −0.481 |
| 0.28 | 11.01 | 0.511 | −0.483 |
| 0.35 | 8.80 | 0.557 | −0.485 |

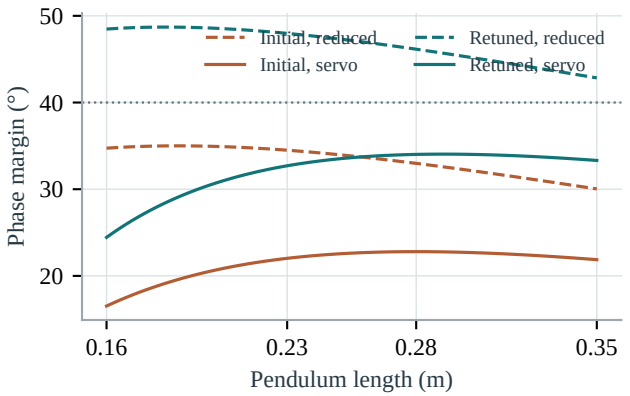


**Figure 7.3** – Phase margin at 77 lengths for both designs and both models. The original reduced-design target is marked at 40°. The cart-servo curves depart most from their reduced counterparts at short length.

The nominal retuned modulus margin of 0.557 drops to about 0.290 at 0.16 m with the same cart model. The corresponding delay threshold drops from 66.1 to 21.8 ms. These trends are consistent with the higher crossover. They expose a substantial loss of reserve even though the model remains linearly stable and its steady sine tracking is exact at the designed frequency. The retuned retained phase curve has a broad interior maximum, so comparing only the two endpoint margins would miss the small turning point.

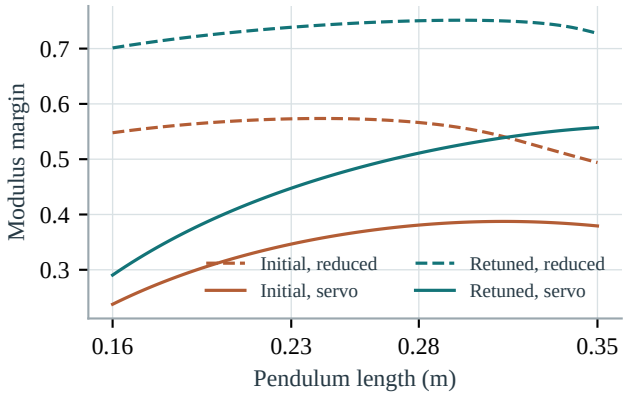


**Figure 7.4** – Modulus margin over the nominal-servo length interval. Shorter lengths show a sharper decline when the cart dynamics are retained.

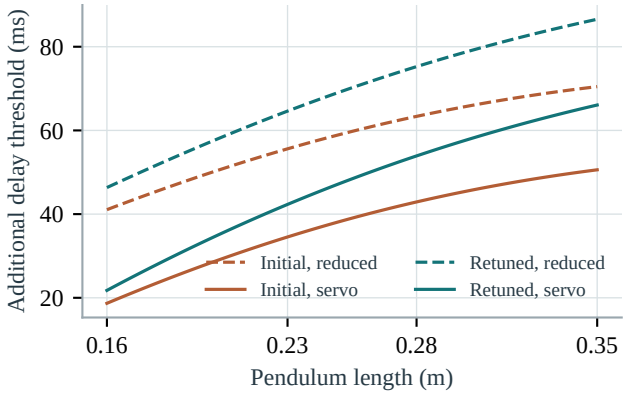


**Figure 7.5** – Pure-delay threshold over length. The same component of phase reserve corresponds to a smaller time delay at a higher crossover.

The result supports two distinct statements. One concerns linear stability over a continuous interval of lengths with one nominal cart servo. The other concerns frequency-domain reserve conditional on that operating point. Numerical refits of the controller at every length, linear convergence of a time trace, or absence of a 5 V excursion in one run cannot substitute for these comparisons.

## 7.4 Joint uncertainty in the identified servo

The two estimates in Section 3 motivate a separate test in which $\omega_c/\omega_{c0}$ takes seven evenly spaced values from 0.85 to 1.15 and $\zeta$ takes seven from 0.38 to 0.62. The script evaluates 21 equally spaced lengths in the original interval. The Cartesian product contains 1,029 configurations for each tuning. Closed-loop spectral abscissae are computed with identical coefficients inside each set. All tested points have negative abscissa, and Table 7.3 identifies the worst grid point for each design.

**Table 7.3** – Largest real part reached in each 1,029-point servo uncertainty test.

| RST | $\sigma$ ($s^{-1}$) | L (m) | $\omega_c$ (rad/s) | $\zeta$ |
|---|---|---|---|---|
| Initial | −0.852 | 0.35 | 43.92 | 0.62 |
| Retuned | −0.473 | 0.16 | 43.92 | 0.62 |

The minimum tested frequency is approximately 43.92 rad/s. The two worst abscissae occur at this frequency and $\zeta = 0.62$, but at different lengths. The grid is deliberately a deterministic stress test. The lengths and servo settings between its nodes, and dynamic behavior outside the chosen second-order servo family, require additional analysis. The result also cannot isolate the effect of sensor dynamics or friction because these were not parameters in the grid.

## 7.5 Reassessment of the original pole-allocation strategy

The original tuning guidance orders the rates qualitatively as $\beta \ll \alpha \ll \gamma \ll \omega_c$. Its retuned value $\gamma = 30\ s^{-1}$ is about 58% of $\omega_c$, a modest separation from the cart frequency. The source reports a search for the chosen pair but supplies no complete candidate inventory. A new, explicit comparison covers nine $\beta$ values from 0.25 to 2.0 $s^{-1}$ and eleven $\gamma$ values from 6 to 50 $s^{-1}$. Each of the 99 candidates is synthesised at 0.35 m and then assessed with the retained servo at all four source lengths.

For each candidate define the minimum phase margin and minimum modulus margin across those lengths. Also evaluate the zero-state demand just after a +0.40 V measurement edge. Its magnitude is $0.40|r_0|$, as proved in Section 8.4. This inexpensive diagnostic exposes direct control demand which a Bode margin alone cannot describe. The metric applies to the leading jump. The subsequent command can have a larger peak, as it does for the archived retuned controller.

$$\phi_{\min} = \min_{L \in \mathcal{L}_4} \phi_m(L),$$
$$M_{\min} = \min_{L \in \mathcal{L}_4} M_m(L) \qquad (7.4)$$
$$J_b = 0.40\,|r_0|$$

Every candidate is linearly stable at the four tested lengths and has one descending unity-gain crossing there. The best minimum margin on this grid is about 30.70° at (β,γ)=(0.25,50). The same grid point has the highest minimum modulus margin, 0.326. Its instantaneous command demand for the test edge is 9.01 V, outside the ±5 V band. Among points with $J_b \le 5$ V the largest minimum phase margin is about 26.03° at (0.25,25), with 4.96 V initial demand and a slowest real part near $-0.241\ s^{-1}$. The grid therefore shows a trade-off even before enforcing the rest of the transient.

**Table 7.4** – Two archived tunings and two selected grid points. The last column gives the demand at the measurement edge.

| β | γ | Min. $\varphi_m$ (°) | Min. $M_m$ | Edge (V) |
|---|---|---|---|---|
| 1.00 | 10 | 16.52 | 0.238 | 3.235 |
| 0.50 | 30 | 24.44 | 0.290 | 6.213 |
| 0.25 | 50 | 30.70 | 0.326 | 9.007 |
| 0.25 | 25 | 26.03 | 0.324 | 4.961 |

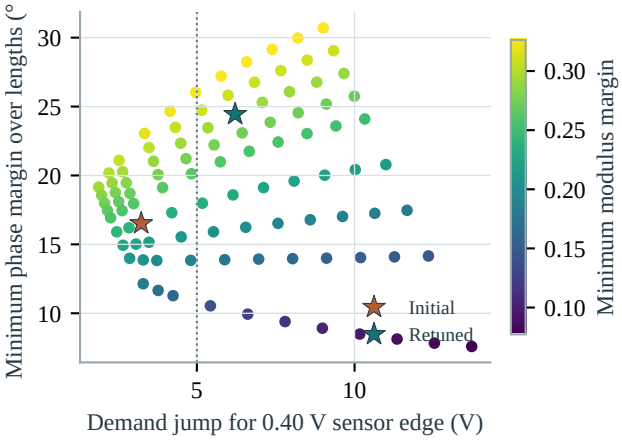


**Figure 7.6** – Four-length comparison on the 99-point pole-allocation grid. Color gives the worst modulus margin. Stars identify the two archived tunings. The vertical line marks the 5 V demand criterion for the specified edge only.

Within the sampled set the 40° minimum from the reduced design is not reached on the model that retains the servo. The grid cannot exclude other pole assignments, a higher-order RST synthesis, a filtered measurement path or a different performance specification. Its main value is to show which of the original design metrics compete once servo dynamics and a fast measurement perturbation are evaluated together.

# 8 Reproducible linear and limited-command experiments

## 8.1 State model, time grid and metrics

The models use the controller realisation in Appendix A. For the retained plant use states $x_m, \dot{x}_m, \eta, \dot{\eta}$. Here v denotes the cart servo input, including any additive input disturbance. The controller computes u from r and z, and the limiter acts on u before $d_u$ is added. Its ideal hard bounds are the simulation assumptions. The cart and pendulum equations use a common time origin and continuous states.

$$\begin{aligned} u_a &= \min(5, \max(-5, u)), \quad v = u_a + d_u \\ \ddot{x}_m &= \omega_c^2 (v - x_m) - 2\zeta\omega_c \dot{x}_m \\ \ddot{\eta} &= \lambda\eta - \ddot{x}_m, \\ y &= x_m + \eta, \quad z = y + b \end{aligned} \tag{8.1}$$

For the second-order realisation with the servo replaced by unity, $x_m$=v and the plant can be integrated directly in output coordinates. With zero initial conditions it has the transfer $H_2$ of equation (3.18). This formulation avoids differentiating a discontinuous v in software. The nonlinear model of Section 9 is obtained from the retained state model. Each experiment specifies its model, forcing and terminal condition.

$$\begin{aligned} \ddot{y} &= \lambda(y - v) \\ \frac{Y}{V} &= \frac{-\lambda}{s^2 - \lambda} \end{aligned} \tag{8.2}$$

The SciPy DOP853 solver restarts on the prescribed switching edges. It uses relative tolerance $10^{-9}$, absolute tolerance $10^{-11}$, maximum internal step 25 ms and an output grid of 5 ms. Initial states are zero except in the finite-angle tests. The same limiter is applied to the controller demand in every bounded run. No additional integrator feedback is used for anti-windup, and the model contains no travel stop, rate limit or friction law. Thus the experiment isolates the ideal command-amplitude bound.

The tracking error is y − r in the reference-only experiment, where y equals z. For the input and sensor pulses the performance output is the physical y before the additive sensor term. The band-return metric uses the last time sample outside ±20 mV, then the first remaining sample. This computes return relative to a specified reference edge or pulse removal. It uses a finite observation horizon and gives a discrete value rather than a continuous-time crossing estimate.

$$\begin{aligned} I_e &= \{ i : t_i \geq t_e,\ |e(t_j)| \leq b_e \text{ for all } j \geq i \} \\ t_r &= t_{\min I_e} - t_e, \qquad b_e = 0.02 \text{ V} \\ \text{IAE} &= \int_0^{T_h} |e(t)|\, dt \end{aligned} \tag{8.3}$$

In addition report the maximum sampled magnitude of y or u and the terminal-window error RMS where appropriate. The command-demand peak and applied-command peak are both retained when the limiter is active. Clipping duration is an integration of the sampled limiter indicator. These choices allow quantitative comparison and give a way to reproduce every time-domain value below.

## 8.2 E1: Reconstructed reference without an added disturbance

The first test starts from rest, runs to 30 s and applies the unit sine and offset change inferred in Section 6. There is no added input disturbance or sensor pulse. The reference is continuous at sine onset t = 5 s, with a change in its derivative. At t = 15 s it jumps by 1 V.

$$\begin{aligned} r(t) = \mathbf{1}_{t \geq 5} &\sin[\omega_0 (t - 5)] \\ &+ \mathbf{1}_{t \geq 15} \quad \text{V} \end{aligned} \tag{8.4}$$

At the design frequency the interpolation gives $U/R_f = A/B$. For the retained model at $j\omega_0$, this becomes $D_c(j\omega_0)(1+\omega_0^2/\lambda)$. At L = 0.35 m its magnitude is about 1.036. At zero the gain is one. Thus the expected command after transients is close to a unit offset plus a 1.04 V sine. The early part of the trajectory can have a larger excursion, and the controller feedthrough also introduces a negative command jump at the positive reference step.

$$\left.\frac{U}{R_f}\right|_{s=0} = 1$$
$$\left.\frac{U}{R_f}\right|_{s=j\omega_0} = D_c(j\omega_0)\left(1+\frac{\omega_0^2}{\lambda}\right) \tag{8.5}$$

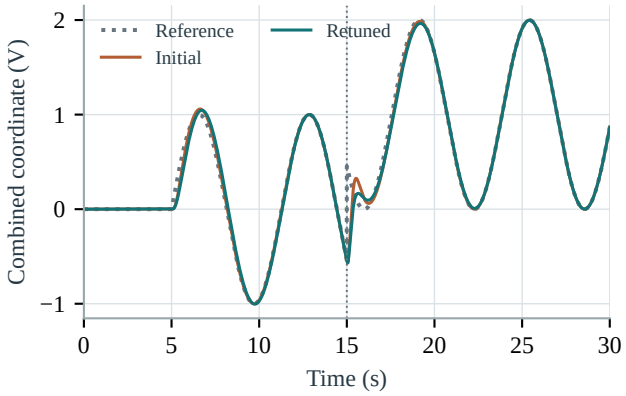


**Figure 8.1** – Reconstructed E1 reference and combined output at L = 0.35 m with the cart servo retained. The two tunings nearly coincide away from the two reference changes.

The plotted output is close to the reference over most of the horizon. That alone hides the response to the offset change. At 15 s the error jumps to roughly −1 V because the reference is discontinuous and the plant strictly proper. The initial and retuned errors then have different oscillatory tails. The direct command contribution immediately after the edge equals the leading T coefficient times the jump, so the visible command discontinuity is expected under either tuning.

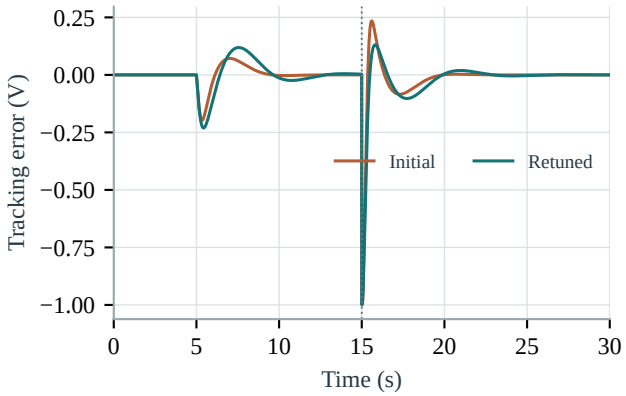


**Figure 8.2** – Full E1 tracking error. The large excursion aligns with the +1 V step. The error at sine onset is much smaller.

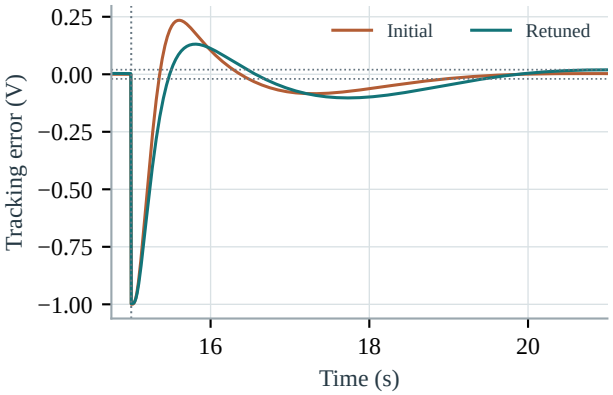


**Figure 8.3** – E1 tracking-error detail after the offset change. The dotted horizontal lines mark the ±20 mV band used for the sampled return metric.

The retuned response stays nearer the band during part of the early transient, yet crosses and leaves the band later. The band return from t = 15 s is 3.96 s with the initial retained model and 4.44 s with the retuned retained model. The retuned reduced model takes 6.36 s by the same criterion. This large change in a narrow-band metric between two models is consistent with their different transient combinations. The maximum error around the step and the tail error over 25–30 s measure different parts of the curve.

**Table 8.1** – Nominal E1 response. Error RMS is over 25–30 s. Band return is measured from the 15 s reference step.

| RST | Plant | Peak u (V) | RMS (mV) | Return (s) |
|---|---|---|---|---|
| Initial | $H_2$ only | 2.355 | 0.011 | 3.85 |
| Initial | $H_1H_2$ | 2.371 | 0.026 | 3.96 |
| Initial | Nonlinear | 2.371 | 0.031 | 4.10 |
| Retuned | $H_2$ only | 2.034 | 0.895 | 6.36 |
| Retuned | $H_1H_2$ | 2.034 | 0.974 | 4.44 |
| Retuned | Nonlinear | 2.034 | 0.952 | 4.48 |

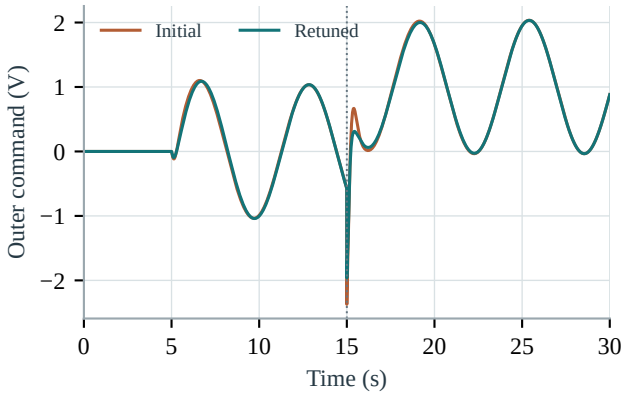


**Figure 8.4** – E1 outer command at nominal length. Demand equals applied command because the 5 V limiter is inactive on these reference-only trajectories.

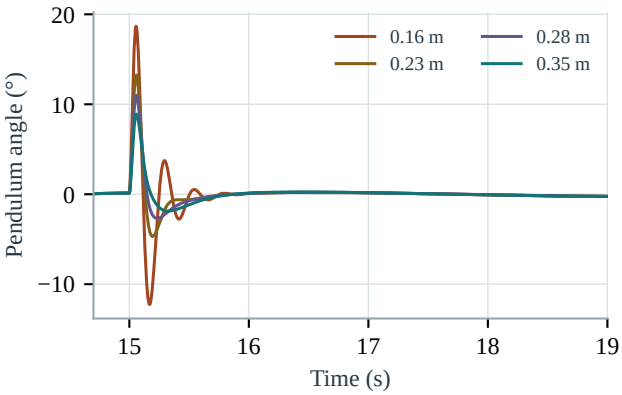


**Figure 8.5** – Calculated E1 angular responses near the step, for all four lengths with the same retuned RST and the illustrative position-to-voltage scale.

The initial retained model reaches a sampled demand of about 2.371 V. The retuned value is 2.034 V, a reduction of approximately 14.2%. The RMS errors in the 25–30 s window are 0.026 mV and 0.974 mV. A slower small-amplitude transient can raise the latter number despite exact asymptotic sine tracking in both retained linear loops. The nonlinear nominal calculation is close for this excitation under the assumed scale, as Table 8.1 shows, and the limit is inactive in all six nominal comparisons.

**Table 8.2** – E1 with the same retuned controller at four lengths. Angle peaks use the assumed calibration.

| L (m) | Peak u (V) | Peak \|θ\| (°) | Band return (s) |
|---|---|---|---|
| 0.16 | 2.014 | 18.68 | 6.34 |
| 0.23 | 2.021 | 13.25 | 6.20 |
| 0.28 | 2.026 | 11.01 | 4.47 |
| 0.35 | 2.034 | 8.90 | 4.44 |

With the retuned controller the four retained-model peaks are 2.01410, 2.02129, 2.02641 and 2.03358 V. The respective archived numbers are 2.0142, 2.0213, 2.0265 and 2.0336 V. The agreement of these scalars, combined with the visible green reference, supports the reference reconstruction. Complete equality to the archived Simulink run would require its initialisation, additive signals and block settings.

The narrow range of command peaks across length coexists with a factor of about 2.10 between reconstructed angular maxima at the endpoints. The second derivative identity (3.19) explains why a larger angular peak can occur in the short transient even though the settled sine angle is length-independent at fixed scale, amplitude and frequency. Angular traces can therefore distinguish conditions obscured by a full-window overlay of combined positions.

## 8.3 E2: Independent cart-input pulse

Set r = b = 0 and apply $d_u$ = +0.50 V over 15≤ t<15.5 s. The pulse enters at the input to $H_1$, so it is in the cart-position voltage coordinates. The experiment compares the BS/P channel from Section 2, with the limiter available but inactive. Changing the amplitude or pulse length would generally change the peak and band-return metrics.

The retained transfer $H_4$ has relative degree four. With a zero state at the first edge, the cart acceleration jumps but the angular contribution initially cancels it in $\ddot{y}$. The first nonzero short-time term in y arises at order four. This yields the initially smooth negative motion in Figure 8.6 even though the applied pulse is positive. The sign is a consequence of the upright convention and the negative numerator in $H_2$.

$$\ddot{x}_m(0^+) = 0.50\,\omega_c^2,$$
$$\ddot{\eta}(0^+) = -0.50\,\omega_c^2$$
$$y^{(4)}(0^+) = -0.50\,\lambda\omega_c^2 \qquad (8.6)$$
$$y(t) = -\frac{0.50\,\lambda\omega_c^2}{4!}t^4 + o(t^4)$$

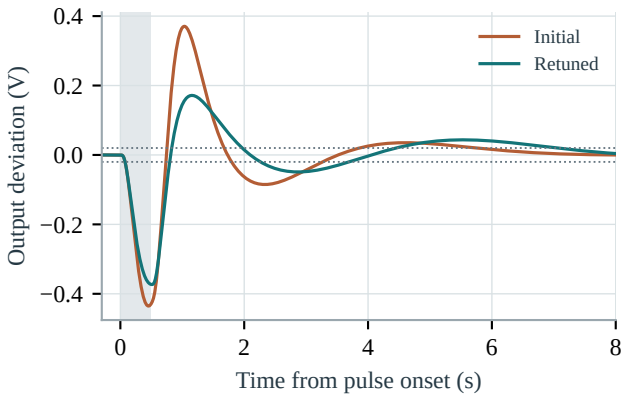


**Figure 8.6** – Nominal-length E2 comparison. Time zero is the input-pulse edge. The shaded pulse lasts 0.50 s and the dotted levels give the output band.

The initial design reaches about 0.435 V of output deviation and the retuned design 0.373 V. Their IAEs are 0.556 and 0.474 V·s. These are reductions of roughly 14% and 15%. The retuned deviation returns to the band in 6.55 s, compared with 5.25 s for the initial design, measured after removing the excitation. A lower peak and longer terminal tail are observable together. The ranking of the two controllers therefore depends on the chosen criterion.

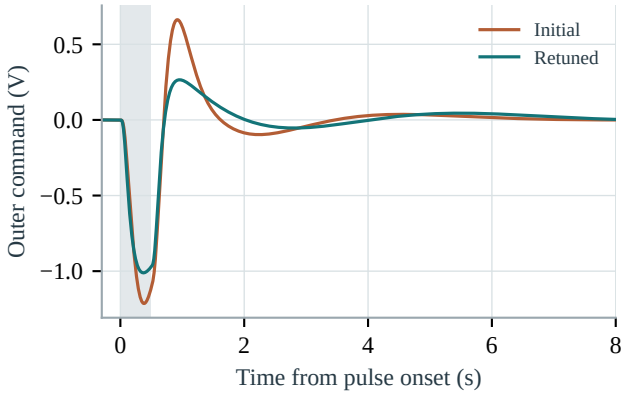


**Figure 8.7** – Nominal outer command during E2. The plotted command is the controller's response before addition of the input pulse. The peak remains within the simulated bounds.

**Table 8.3** – E2 input pulse. Columns I and R use the initial and retuned designs. Band return starts at pulse removal.

| L (m) | Peak I (V) | Peak R (V) | Return I (s) | Return R (s) |
|---|---|---|---|---|
| 0.16 | 0.384 | 0.330 | 5.30 | 6.57 |
| 0.23 | 0.404 | 0.341 | 5.29 | 6.57 |
| 0.28 | 0.419 | 0.355 | 5.27 | 6.56 |
| 0.35 | 0.435 | 0.373 | 5.25 | 6.55 |

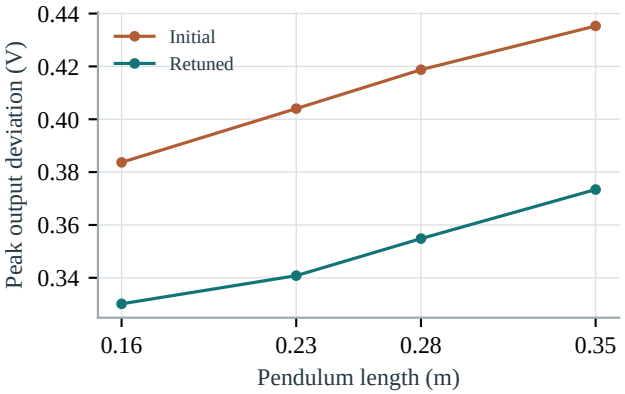


**Figure 8.8** – E2 peak deviation over the four source lengths. This variation concerns the explicitly defined servo-input pulse and the retained model.

All four retuned output peaks are smaller than the corresponding initial values under this input. The retained model's peak deviations increase modestly with length, even though the shortest pendulum has the higher angular instability rate. The short-time coefficient in equation (8.6) increases as L falls, while the final peak depends on the poles and zeros of the entire closed loop. A local expansion around the switching instant cannot extrapolate to the later maximum.

## 8.4 E3: Independent measurement pulse

Use $r = d_u = 0$, L = 0.35 m and add b = +0.40 V over $5 \le t < 5.5$ s. At either edge the plant output and controller states are continuous, while their algebraic outputs can contain a feedthrough. If $t_{lead}$ is the $s^4$ coefficient of T, the proper controller in equation (2.3) gives the demand jump $\Delta u = t_{lead}\Delta r - r_0\Delta b$ for this isolated sensor case. It follows by evaluating the direct-feedthrough limit as $s \to \infty$, or by inspecting the final row of the shared realisation.

$$\lim_{s\to\infty}\frac{T}{S}=t_{\text{lead}},\qquad \lim_{s\to\infty}\frac{-R}{S}=-r_0 \qquad \Delta u=t_{\text{lead}}\Delta r-r_0\Delta b \tag{8.7}$$

Starting from zero demand, the instantaneous edge thresholds for the initial and retuned designs are 5/8.0884=0.6182 V and 5/15.5321=0.3219 V. The chosen +0.40 V step therefore gives +3.235 and +6.213 V just after onset. With a nonzero prior u, the distance to the relevant limit also depends on its sign and level. Even when the edge is below threshold, later dynamics may still cause a limit event.

$$|b_{\text{edge}}|\le\frac{5}{|r_0|} \qquad (u(0^-)=0,\ \Delta r=0) \tag{8.8}$$

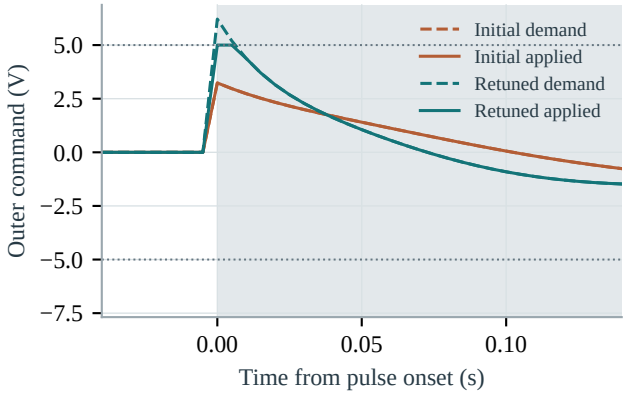


**Figure 8.9** – Early demand and applied command for the E3 measurement pulse. The retuned demand exceeds the limit and continues to change while the applied signal is clipped.

The complete simulated retuned demand peaks at 7.019 V with no limit and 7.023 V under the ±5 V limiter. Clipping in the latter case lasts approximately 25 ms by the sample-based metric. The initial controller peaks at 4.231 V with either implementation. The maximum demand exceeds the instantaneous jump in both designs, so the edge metric correctly exposes exposure to clipping while underestimating the later peak.

**Table 8.4** – Independent +0.40 V measurement pulse at nominal length. Values in volts.

| RST | Limit | Demand | Applied | Peak \|y\| |
|---|---|---|---|---|
| Initial | None | 4.231 | 4.231 | 0.971 |
| Initial | ±5 V | 4.231 | 4.231 | 0.971 |
| Retuned | None | 7.019 | 7.019 | 0.809 |
| Retuned | ±5 V | 7.023 | 5.000 | 0.805 |

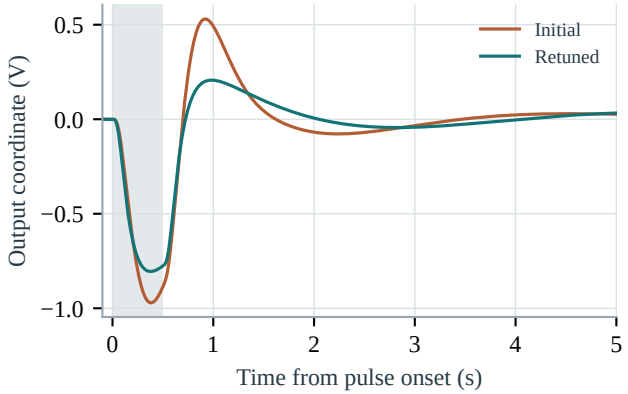


**Figure 8.10** – E3 physical output y before addition of the sensor pulse. A negative first lobe is followed by a positive rebound. Both responses are from the limited-plant simulation.

The retuned limited case has lower maximum physical output deviation, about 0.805 V instead of 0.971 V. Its return interval is longer, about 6.36 s instead of 4.96 s after pulse removal. The difference between measured and physical output is exactly the specified corruption during the pulse. Evaluating only the signal used in feedback could obscure which output was actually displaced. This test is much larger than a small-signal noise-spectrum test, and its purpose is to expose the command feedthrough under one documented perturbation.

## 8.5 E4: Robustness to frequency detuning

The internal model sets the zeros of the reference error transfer at exactly 0 and $\pm j\omega_0$. It does not impose an interval of perfect tracking around $\omega_0$. With $Q_e=(T-R)/F_i$, equation (4.10) gives $G_e(j\omega)$ for any nearby frequency. For a 1 V pure sine its steady RMS error is $|G_e(j\omega)|/\sqrt{(2)}$, and the corresponding command amplitude is $|AT/P|$. The abrupt change of r in E1 is absent here.

$$G_e(j\omega) = \frac{F_i(j\omega)[BQ_e - AQ](j\omega)}{P(j\omega)}$$
$$E_{\mathrm{rms}}(\omega) = \frac{1}{\sqrt{2}}|G_e(j\omega)| \tag{8.9}$$
$$U_{\mathrm{amp}}(\omega) = \left|\frac{A(j\omega)T(j\omega)}{P(j\omega)}\right|$$

Differentiating $F_i = s(s^2+\omega_0^2)$ gives $F_i'(j\omega_0) = -2\omega_0^2$. Because $F_i$ is zero at the design point, terms from the derivatives of A, B and P drop out of the first-order expansion. The local slope grows when the residual polynomial in the numerator is large relative to the closed-loop value of P. The derivative yields a local linear dependence in $|\omega-\omega_0|$ when the coefficient is nonzero. Asymmetry farther from the notch comes from additional frequency dependence.

$$\left.\frac{dG_e(j\omega)}{d\omega}\right|_{\omega_0} = jF_i'(j\omega_0)\frac{(BQ_e - AQ)(j\omega_0)}{P(j\omega_0)} \tag{8.10}$$
$$F_i'(j\omega_0) = -2\omega_0^2$$

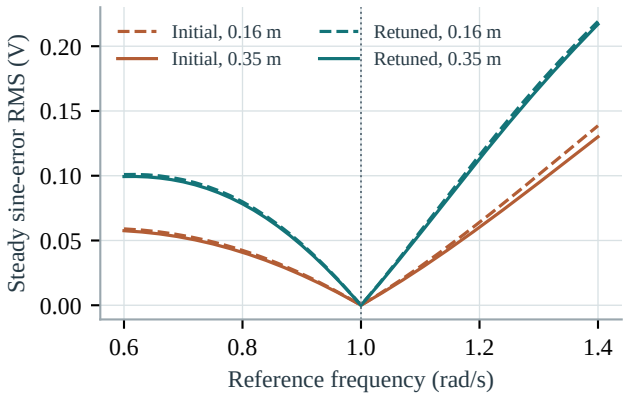


**Figure 8.11** – Calculated RMS tracking error for a 1 V unit sine across frequency. Solid lines use L = 0.35 m and dashed lines 0.16 m. Both retain the cart servo.

At 0.85 and 1.15 rad/s the nominal retuned RMS errors are approximately 64.2 and 84.3 mV. These values are large relative to the late E1 transient RMS, since the forcing persists away from the internal-model frequency. The use of one internal model primarily fixes the notch location. The width and shape of the notch remain design- and plant-dependent.

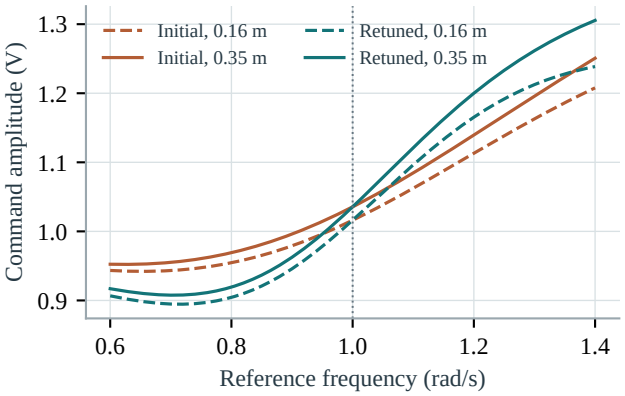


**Figure 8.12** – Steady command amplitude for the same detuning experiment. Frequency-selective output error need not coincide with a large command amplitude.

**Table 8.5** – Frequency detuning check at nominal length. Fitted values use the 50–64 s simulation window.

| ω (rad/s) | Predicted (mV RMS) | Fitted (mV RMS) |
|---|---|---|
| 0.85 | 64.202 | 64.202 |
| 1.00 | 0.000 | 0.000 |
| 1.15 | 84.324 | 84.324 |

As a separate numerical check, the retuned nominal model was integrated for 64 s at 0.85, 1.00 and 1.15 rad/s. Sine, cosine and constant terms were fitted to the last 14 s of error, which avoids assuming the window is an integer number of periods. The harmonic magnitudes agree with (8.9) within $2\times10^{-12}$ V in these runs, and the limiter is inactive. The check compares two computational representations of the same model and provides an implementation test for the reconstructed tracking result.

# 9 Finite-angle response and calibration dependence

## 9.1 Pendulum equation with the identified cart

The nonlinear scenario retains the cart servo and uses the exact trigonometric terms from the second line of (3.4). It continues to combine the scaled angular and cart coordinates as in the simulated measurement. The link between the servo and pendulum is through $x_m$". Cart reaction, friction and a geometric travel constraint remain outside this cascade. The construction therefore tests how much the existing controller changes when linear gravitational and acceleration projection terms are relaxed.

$$\begin{aligned} \theta &= \frac{\eta}{K_x L}, \\ \ddot{\eta} &= K_x g \sin\theta - \ddot{x}_m \cos\theta \\ \ddot{y} &= K_x g \sin\theta + \ddot{x}_m (1 - \cos\theta) \end{aligned} \tag{9.1}$$

Equation (9.1) recovers ÿ=λη at first order. At finite angle the output curvature also depends on cart acceleration. Thus the linear steady-angle formula (3.19) is a local prediction. The geometric difference between the controlled signal and scaled bob displacement also increases, as (3.17) shows. These are two distinct departures from the linear approximation.

Scale time by υ=α t. Primes in equation (9.2) denote derivatives in υ. The same normalized gravitational acceleration acts at a given angle, but the same number of physical seconds passes through more unstable time constants for short L. The apparent inertial torque depends on the cart acceleration relative to g. It is therefore useful to compare both angle and trajectory time, not angle alone.

$$\begin{aligned} \theta''(\upsilon) &= \\ \sin\theta - \frac{\ddot{x}}{g}\cos\theta, \\ \alpha &= \sqrt{\frac{g}{L}} \end{aligned} \tag{9.2}$$

For the angular dynamics under prescribed cart acceleration, the pendulum energy relative to a translated pivot, per unit bob mass, is $E_b = L^2\dot{\theta}^2/2 + gL\cos\theta$. Its rate of change follows from multiplying the angular equation by $L\dot{\theta}$. Actuation can remove or add energy depending on the sign of cart acceleration and angular velocity. The saturation interval and reversal phase therefore matter in addition to the initial value of θ.

$$\begin{aligned} \mathcal{E}_b &= \frac{L^2}{2}\dot{\theta}^2 + gL\cos\theta \\ \frac{d\mathcal{E}_b}{dt} &= -L\dot{\theta}\ddot{x}\cos\theta \end{aligned} \tag{9.3}$$

## 9.2 What the archived angles imply for the approximation

For a nonzero angle the relative error incurred by replacing sinθ by θ can be referenced to the linear term, giving 1−sinθ/θ. The fractional reduction in the acceleration projection relative to unity is 1−cosθ. Both depend only on the instantaneous angle, in radians. Taylor expansion gives separate leading coefficients for the two errors.

$$\begin{aligned} \varepsilon_g &= 1 - \frac{\sin\theta}{\theta} \\ &= \frac{\theta^2}{6} + O(\theta^4) \\ \varepsilon_a &= 1 - \cos\theta \\ &= \frac{\theta^2}{2} + O(\theta^4) \end{aligned} \tag{9.4}$$

**Table 9.1** – Relative gravity-term error and lost fraction of cart-acceleration projection at archived angle magnitudes.

| \|θ\| (°) | Gravity (%) | Projection (%) |
|---|---|---|
| 14.30 | 1.04 | 3.10 |
| 17.56 | 1.56 | 4.66 |
| 31.33 | 4.91 | 14.58 |

At 14.30° the two differences are about 1.04% and 3.10%. At 31.33° they are about 4.91% and 14.58%. In the latter case taking the projected cart acceleration to be its full value has a much larger effect than the gravity approximation alone. In the full force-driven translation equation, the centrifugal term cannot be deduced from peak angle. For

$\theta\cos\theta \neq 0$, its magnitude relative to the angular-acceleration coupling is

$$\frac{|mL\dot{\theta}^2 \sin\theta|}{|mL\ddot{\theta}\cos\theta|} = \frac{\dot{\theta}^2}{|\ddot{\theta}|}\,|\tan\theta|. \tag{9.5}$$

The ratio depends on instantaneous angular velocity and acceleration. At an interior angular maximum the velocity term vanishes, while it may be appreciable at other phases of the motion. A tolerance for individual terms also does not by itself bound trajectory error over a closed-loop transient.

## 9.3 E5: Initial-angle experiments with the command limit

Each run starts with $x_m = 0$, zero velocities and zero controller state, with $\eta(0) = K_x L \theta_0$. The retuned coefficients stay fixed and r, $d_u$ and b are zero. The event stops integration when $|\theta| = 45°$, or the run reaches 14 s. The event is a reporting boundary for this model, placed outside the region of primary interest. A run ending at it supplies its hitting time and preceding peaks.

$$u(0^+) = -r_0 K_x L \theta_0 \qquad |\theta_{\text{edge}}| = \frac{5}{|r_0| K_x L} \tag{9.6}$$

The nominal illustrated scale of 24 V/m and the retuned $r_0$ give a 2.20° initial clipping threshold at 0.35 m and 4.80° at 0.16 m. These thresholds describe only the starting command. A small initial angle for the short pendulum can start below the limit and later encounter it. Conversely, an initially clipped trajectory can recover enough cart authority as its phase changes.

**Table 9.2** – E5 initial-angle trials with $K_x$ = 24 V/m. Event times refer to the first $|\theta|$ = 45°.

| L (m) | $\theta_0$ (°) | Peak $\lvert\theta\rvert$ (°) | $\lvert x\rvert$ (cm) | Event (s) |
|---|---|---|---|---|
| 0.35 | 2.0 | 15.38 | 10.5 | — |
| 0.35 | 5.0 | 45.00 | 28.1 | 0.797 |
| 0.35 | 8.0 | 34.52 | 27.5 | — |
| 0.16 | 0.5 | 3.60 | 1.1 | — |
| 0.16 | 1.0 | 7.84 | 2.4 | — |
| 0.16 | 2.0 | 45.00 | 15.6 | 0.281 |

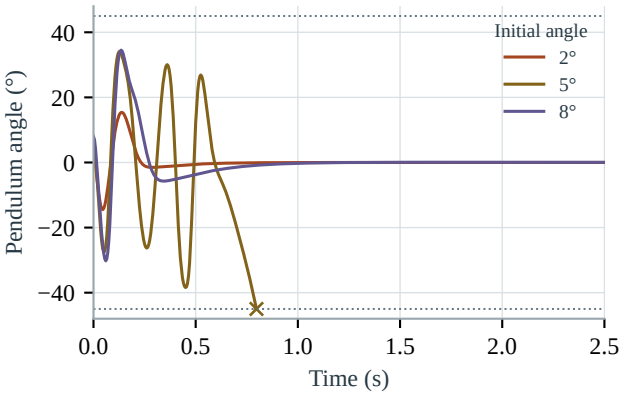


**Figure 9.1** – First 2.5 s of the finite-angle trajectories at 0.35 m. Crosses mark the first 45° cutoff. The remaining trajectories continue to 14 s.

At nominal length the 2° case peaks near 15.38° of opposite-sign swing magnitude and remains below 5 V. The 5° case reaches the cutoff at about 0.797 s. The 8° case initially clips, reverses before the cutoff and reaches a peak magnitude of about 34.52°. It returns close to upright by 14 s. The three curves demonstrate a nonmonotone outcome in this one-dimensional slice of initial conditions. Their differences are also visible in the timing and duration of applied-command clipping in Figure 9.3.

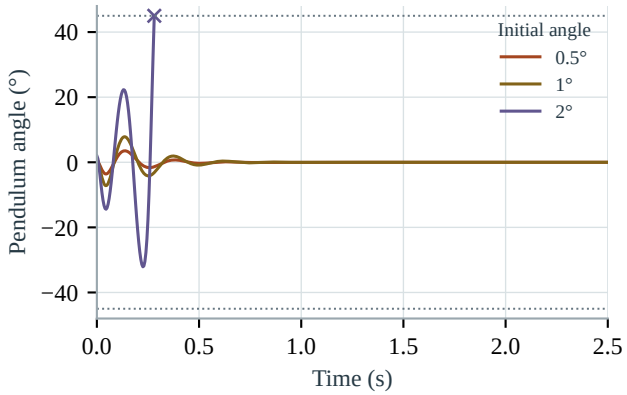


**Figure 9.2** – Finite-angle runs at 0.16 m with the same retuned RST. The 2° trial reaches the cutoff at about 0.281 s.

At 0.16 m both 0.5° and 1° initial offsets remain within the command limit and converge in the model. At 2° the short-length trajectory reaches the cutoff despite starting below its calculated initial edge limit. The limited-command behavior therefore cannot be predicted by a criterion on initial |u| alone. The cut-off long and short runs also have substantial cart displacements by their last samples. A real limit on travel could intervene earlier or change an apparently recovered trajectory.

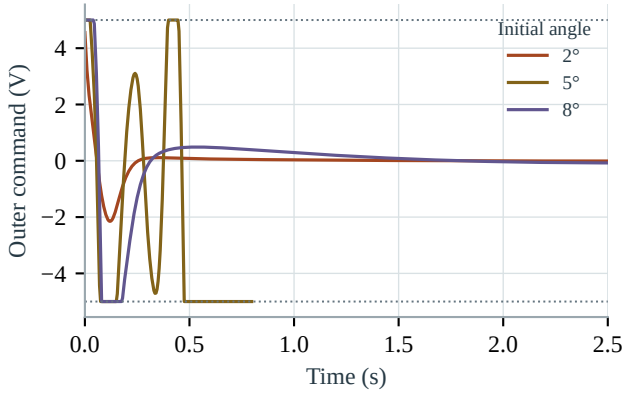


**Figure 9.3** – Applied outer command for the three nominal-length initial-angle trials. Plateaux at ±5 V mark ideal clipping. Command history differs substantially between the 5° and 8° trials.

## 9.4 Scaling the finite-angle test

The dependence on $K_x$ can be seen by introducing $u_x=u_a/K_x$ and $x=x_m/K_x$. For zero reference and disturbances, the normalized mechanical equations are unchanged if coordinates and controller states are expressed per unit $K_x$. The physical command range of those rescaled equations becomes $5/K_x$. Hence these changes in $K_x$ also alter how much position-command range is available. The numerical sweep tests 18, 24 and 30 V/m, without treating these points as calibration measurements.

$$\begin{aligned} \ddot{x} &= \omega_c^2(u_x - x) \\ &-2\zeta\omega_c\dot{x}, \quad |u_x| \le \frac{5}{K_x} \\ y/K_x &= x + L\theta \end{aligned} \tag{9.7}$$

**Table 9.3** – Stopping times in seconds for three illustrative scale factors $K_x$. A dash denotes no 45° event within 14 s.

| L (m) | $\theta_0$ (°) | 18 V/m | 24 V/m | 30 V/m |
|---|---|---|---|---|
| 0.35 | 8.0 | 0.221 | — | 0.687 |
| 0.35 | 5.0 | — | 0.797 | — |
| 0.16 | 2.0 | 0.279 | 0.281 | 0.285 |

The 5° nominal trial reaches the cutoff for 24 V/m and stays below 45° at both 18 and 30 V/m in the tested interval. For 8° the cutoff status changes in the opposite way at these three scales. At 0.16 m and 2° all three runs hit the cutoff near 0.28 s. This comparison highlights the unreliability of inferring a capture angle from a few isolated outcomes. The experiment is a set of trajectory checks with defined initial states; a region-of-attraction result would also vary initial velocity, cart position, controller state and physical constraints.

The event time changes by about 4 µs for the nominal 5° case and less than 1 ns for the short 2° case when the output grid is halved and the solver tolerances tightened as described in Appendix B. Those differences are smaller than the effects of changing scale or length. The numerical event tolerances therefore do not explain the changes of outcome in Table 9.3.

# 10 Interpretation and experimental checks

## 10.1 What the comparisons establish

The Bézout construction restores the internal model and all six nominal target modes from explicit coefficient equations. It reproduces the initial and retuned reduced-model frequency margins and identifies a sign error in the initial $r_2$ transcription. Retaining the cart changes the characteristic polynomial to order eight. The shift in crossover and the extra servo phase account for the reduction in the reported margin. A stable characteristic polynomial supports statement of local linear behaviour in a specified model; a margin quantifies the reserve for a specified class of perturbations.

The archived plots support observation of close tracking and comparatively small outer commands for the tested reference sequence. The opening preparation transient and the step in the reference are visible. Correct interpretation requires maintaining the distinction between y and z, and between the edge at t = 15 s and the position from which its response is measured. The retuned angular annotation changes the late peak from the previously quoted 15.05° to 14.30°. A relative comparison is valid at those displayed points, whereas the settling-time comparison would need retained data and a stated tolerance.

The numerical experiments clarify why the type of input matters. A reference-only run has demand well inside the command bound for both designs. The cart-input pulse primarily distinguishes peak deviation and later recovery. The measurement pulse directly loads the R channel and exceeds the command bound under the retuned controller. The detuning test makes the theoretical internal-model restriction measurable. The nonlinear scenarios show how command saturation and calibration can change excursion ordering even for one fixed controller.

## 10.2 Limiting assumptions

The cart servo is identified from two approximate extrema of one trace. A discrepancy between the peak-ratio and first-peak fits makes it useful to measure multiple rising and falling edges. At the same operating point the actual motor drive, servo reference and encoder position would be logged separately; this enables detection of encoder filtering, asymmetric gains, travel effects and delayed drive. Estimating effective inertia involves the bob, link and fixture. Without those measurements the coupling model in (3.5) cannot be tied to the bench response.

For the disturbance study the key measurements are r, the physical output combination before any additive term, z, the demand u, the applied command and both sensor channels. Logging the forcing sequence itself separates input disturbance from output or measurement disturbance. The measured post-step settling time should specify the band, the reference used in the subtraction and the sustained window. Reusing that definition with the simulated input would make a quantitative comparison possible.

The cart speed, actuator force ceiling, travel and sensor units constrain the finite-angle test. The assumed 24 V/m used here can be replaced by a calibration obtained from simultaneous displacement and encoder readings. A finite-angle test of the cascade would then match released initial angle and velocity, with known controller state. Coupled force dynamics and friction can be added when an actuator model and mass properties exist.

## 10.3 From a continuous delay margin to a sampled model

The shortest-length pure-delay threshold of about 22 ms makes timing a meaningful sensitivity parameter. A zero-order hold by itself has an approximately half-sample phase lag at low frequency, in addition to an amplitude change. Equation (10.1) is the normalized frequency response of a rectangular hold of duration $T_s$. It can be compared with the return-ratio phase only as part of a model of the actual discretized controller and the timing of the sampled signals.

$$H_{\mathrm{hold}}(j\omega) = \frac{1 - e^{-j\omega T_s}}{j\omega T_s} = e^{-j\omega T_s/2} \frac{\sin(\omega T_s/2)}{\omega T_s/2} \tag{10.1}$$

As an illustrative calculation, at 19.59 rad/s and $T_S$=10 ms the phase of the hold is about −5.61°. An additional full sample of computation delay would add about −11.22°, equivalent to 15 ms in total. The sum is already a substantial share of the 21.8 ms continuous model threshold. Actual placement of the controller poles and local sensor filters can change crossover, so this phase arithmetic is a sensitivity example. The relevant experimental timing data include sample time, total latency, hold implementation and jitter.

$$\Delta\phi_{\mathrm{hold+delay}} \simeq -\frac{3}{2}\omega_g T_s \simeq -16.8^\circ \quad (\omega_g = 19.59,\ T_s = 0.010) \tag{10.2}$$

### 10.4 Model comparison protocol

A matched verification can first identify the unloaded and loaded local servo in voltage coordinates, then evaluate the closed-loop transfer and control demand at each of the four lengths. The existing reduced model, the retained servo model and a measured or coupled model would share the same reference and disturbance definitions. A frequency response around 1 rad/s would test the internal-model notch, whereas the crossover region would test the delay and sensing model. Time plots would show output error, actual angle and both command signals on aligned axes.

The measurements needed to distinguish these hypotheses follow directly from the equations. The force reconstruction in Section 3 requires mass and actuator information. The scalar gain crossing in Section 5 concerns the selected loop break and does not identify hidden constraints. The length and servo stability comparisons concern fixed RST coefficients. Matching each of these conditions prevents an apparent model disagreement from being attributed to a parameter that changed between runs.

## 11 Conclusion

The original continuous-time design is reconstructed from the nonlinear mechanical equations, the identified cart loop and a polynomial internal model. Explicit solutions of the Bézout and feedforward systems recover the two archived RST designs. The derivation corrects the small-angle sign in the source's intermediate equation and the printed sign of the initial $r_2$. The time-history analysis also corrects the retuned angular annotation to 14.30° at 15.05 s.

For the nominal servo family, the polynomial imaginary-axis calculation gives a constant stable root count over 0.16–0.35 m. With the retuned RST, adding the cart dynamics reduces phase margin from 42.8° to 33.3° at 0.35 m. At 0.16 m the retained model gives 24.4° and a pure-delay threshold of 21.8 ms. These margins describe feedback robustness of the linear model under the specified variations.

The reconstructed reference alone produces about 2.034 V peak demand at nominal length. The independent input pulse demonstrates lower peak deviation but a longer return for the retuned controller. The separate measurement pulse reaches about 7.02 V of demand, enough to activate the simulated ±5 V limiter. Detuning and finite-angle simulations show the consequence of changing reference frequency, command scale and initial state. The formulas, graphs and companion

computation give a common basis for checking those observations against a fully specified bench record.

# References

[1] D. Kumar, *RST Polynomial Control of an Inverted Pendulum: Sinusoidal Reference Tracking, Controller Optimization, and Parametric Robustness Assessment*. École Nationale Supérieure d'Arts et Métiers, Paris, engineering project report, 2026, 37 PDF pages, unpublished.

[2] B. A. Francis and W. M. Wonham, "The internal model principle of control theory," *Automatica*, vol. 12, no. 5, pp. 457–465, 1976. 10.1016/0005-1098(76)90006-6.

[3] I. D. Landau, "The R-S-T digital controller design and applications," *Control Engineering Practice*, vol. 6, no. 2, pp. 155–165, 1998. 10.1016/S0967-0661(98)00016-1.

[4] K. J. Åström and R. M. Murray, *Feedback Systems: An Introduction for Scientists and Engineers*, 2nd ed. Princeton University Press, 2021. ISBN 978-0-691-19398-4.

# A Controller coefficients and shared realisation

## A.1 Complete polynomial coefficients

Tables A.1–A.3 give coefficients in descending powers for both tunings. They use the feedback sign $SU=TR_f-RZ$. In each case $S=s(s^2+1)(s+c_1)$; its three roots at the design forcing frequencies are exact. The table precision is for reading. The script computes coefficients from the target product and uses floating-point values before rounding.

**Table A.1** – R coefficients in descending powers. Calculations use unrounded values.

| Power | Initial | Retuned |
|---|---|---|
| 4 | −8.088403 | −15.532074 |
| 3 | −50.089531 | −91.642997 |
| 2 | −51.579972 | −68.488086 |
| 1 | −73.143839 | −102.296624 |
| 0 | −20.000000 | −18.750000 |

**Table A.2** – S coefficients in descending powers. Calculations use unrounded values.

| Power | Initial | Retuned |
|---|---|---|
| 4 | 1.000000 | 1.000000 |
| 3 | 23.588403 | 42.088403 |
| 2 | 1.000000 | 1.000000 |
| 1 | 23.588403 | 42.088403 |
| 0 | 0.000000 | 0.000000 |

**Table A.3** – T coefficients in descending powers. Calculations use unrounded values.

| Power | Initial | Retuned |
|---|---|---|
| 4 | −1.791221 | −1.386691 |
| 3 | −22.009852 | −43.352848 |
| 2 | −45.282791 | −54.342703 |
| 1 | −45.064160 | −54.006476 |
| 0 | −20.000000 | −18.750000 |

The checks use coefficient residuals, not visual agreement between rounded decimals. For the reduced model the code requires the maximum absolute coefficient of $A_0S+B_0R-P_\star$ to be below $10^{-9}$. It then verifies T minus R at 0 and the two imaginary roots of S. Replacing the polynomials by rounded copies can destroy exact conditions at $j\omega_0$, so reproducibility requires starting from the expressions in Section 4.

$$\begin{gathered}\max_{0\le i\le 6}\left|[s^i](A_0S+B_0R-P_\star)\right|<10^{-9}\\ \max_{p\in\{0,\pm j\omega_0\}}|T(p)-R(p)|<10^{-9}\end{gathered}\tag{A.1}$$

## A.2 Why the two inputs share controller states

Write the controller denominator generically as $S=s^4+a_3s^3+a_2s^2+a_1s+a_0$. Take a controllable companion matrix $A_c$ with first row $(-a_3,-a_2,-a_1,-a_0)$, unit subdiagonal and zeros

elsewhere. Let $B_c=(1,0,0,0)^T$. Solving the four rows of $(sI-A_c)v=B_c$ yields equation (A.2).

$$(sI-A_c)^{-1}B_c = \frac{[s^3,\ s^2,\ s,\ 1]^T}{S(s)} \tag{A.2}$$

For a numerator $N_c=n_4s^4+n_3s^3+n_2s^2+n_1s+n_0$, divide by S. The direct term is $D^ctl=n_4$. The strictly proper residual has four coefficients, which form the output row $C(N_c)$ of the controllable companion form. This use of $D^ctl$ for a scalar is local to this derivation; the plant servo denominator remains $D_c(s)$.

$$\begin{gathered} C_j(N_c)=n_{4-j}-n_4a_{4-j}, \\ j=1,2,3,4 \\ D^{\mathrm{ctl}}(N_c)=n_4 \end{gathered} \tag{A.3}$$

Taking the observable dual allows both numerator rows to become input columns while the output becomes $B_c^T$. The resulting four-state system has the desired transfer from each input, even with a limiter downstream. It uses one copy of the denominator modes. A realisation that integrated the two paths separately would need to address the redundant internal-model modes.

$$\begin{gathered} \dot{\mathbf{z}}=A_c^T\mathbf{z} \\ +C(T)^Tr+C(-R)^Tz \\ u=B_c^T\mathbf{z} \\ +D^{\mathrm{ctl}}(T)r+D^{\mathrm{ctl}}(-R)z \end{gathered} \tag{A.4}$$

Here z without bold type is the measured plant signal and z is the four-state controller vector. The implementation verifies each transfer at three nonsingular complex evaluation points. The expression is well posed in the reduced and retained models because the plant is strictly proper and there is no algebraic feedthrough from u to measured output. In the saturating simulations the output of (A.4) is the demand before the limiter.

### A.3 Parallel roles of the original MATLAB steps

The original listings [1, PDF pp. 32–36] first build the six desired roots and then calculate the feedback coefficients. The equations below reproduce the central calculations in a compact MATLAB form for the initial configuration. This mapped excerpt uses the coefficient labels in Section 4. It illustrates the relation between the executable Python polynomials and the archived implementation.

```
L0 = 0.35; lambda = 9.81 / L0;
a = sqrt(lambda); w0 = 1;
beta = 1; gamma = 10;
p = poly([-gamma, -a, -a, -beta, ...
          -beta+1i*w0, -beta-1i*w0]);
S = conv([1 p(2)], [1 0 w0^2 0]);
A = [1 0 -lambda];
AS = conv(A,S);
```

The first two coefficients of the difference vanish by monicity and the choice of S; retaining the trailing five implements the degree bound directly.

```
R = (p(3:end) - AS(3:end))/(-lambda);
F = conv([1 gamma],[1 beta]);
v = polyval(R,1i*w0)/polyval(F,1i*w0);
q2 = R(end)/polyval(F,0);
q1 = imag(v)/w0;
q0 = (q2-real(v))/w0^2;
T = conv(F,[q0 q1 q2]);
```

The source calls the Simulink model to form ymc, ym, u and Theta for each length. That step depends on the actual model and signal data. The companion Python script instead forms A,B and a four-state controller directly and integrates the declared inputs. It preserves equivalent polynomial, frequency and time comparisons where the archived evidence fixes the relevant definitions.

## B Reproducing the numerical results

### B.1 Running the companion script

Use Python with NumPy, SciPy and Matplotlib installed. The run used Python 3.12.14, NumPy 2.3.5, SciPy 1.17.0 and Matplotlib 3.10.8. For an ordinary local environment the simulation command needs only the supplied script and these dependencies. All models, test inputs and constants are defined in the script.

```
python -m pip install numpy scipy matplotlib
python rst_pendule_inverse.py
```

The output folder contains PDF vector figures and numerical records in CSV and JSON. *coefficients.csv* records polynomial coefficients by degree. *frequency.csv* gives nominal metrics at the four lengths and *length_sweep.csv* the 77-point sweeps. *results.json* additionally records complete poles, candidate gain and length crossings, model settings and environment versions.

The file *nyquist.csv* contains the three offset-contour checks at each combination of endpoint length, model and RST. *sensitivity_checks.csv* compares sampled refinement and polynomial stationarity. *retuning_grid.csv* gives every tested β, γ and the three comparison metrics. *servo_uncertainty.csv* gives the worst case from each servo grid. These tables can be used to check the scope of each numerical statement in Sections 5 and 7.

The time-domain summaries are in *reference.csv, pulse.csv, sensor.csv, angle.csv* and *angle_scale.csv*. The detuned sine predictions and harmonic fits are in *detuning.csv* and *detuning_checks.csv*. Rounded values in the report are taken from those computations. The Simulink screenshots are original images copied from their cited pages. They have no direct equivalents in the script's output.

## B.2 Integration checks

The retained retuned E1 run is repeated with a 2.5 ms output grid, relative tolerance $3\times10^{-11}$ and absolute tolerance $3\times10^{-13}$. At common samples the maximum output difference is approximately $2.14\times10^{-11}$ V for the two tolerances. The common-sample comparison samples the denser integration on the original grid; it therefore measures the numerical effect of solver tolerances without adding interpolation error.

For events in E5, the nominal 5° hit and the short 2° hit are recalculated with the same tighter tolerances. The respective event-time changes are approximately $4.0\times10^{-6}$ s and $6.7\times10^{-11}$ s. The former illustrates that the event trajectory contains a crossing near a saturated segment and can be more sensitive numerically than the nominal linear response. These figures are solver checks within one mathematical model. The actual repeatability of a bench trajectory depends on calibrated states, actuator dynamics and measured inputs.

## B.3 Checking a result from the polynomials alone

A short independent check on the command limits is available from the coefficient tables. For the initial design, the $s^4$ coefficient of R is −8.088403 and that of S is one, so the direct path from measured y to u has coefficient +8.088403. For the retuned design it is +15.532074. These quantities give the jump values in Section 8 and can be checked without integrating a trajectory.

A separate check on the nominal phase margin uses the cart denominator evaluated at the reported unity-gain frequency. At 8.80 rad/s, the servo phase is approximately −9.86°. The apparent margin difference of about 9.52° from the reduced to the retained model includes the crossover shift. Comparing these two calculations is a useful way to identify a units or sign error in an independently coded Bode routine.

$$\begin{aligned} 20\log_{10} k_- &\simeq \\ 20\log_{10}(0.64448) &= -3.8158 \text{ dB} \\ \arg H_1(j\,8.80) &\simeq -9.86^\circ \end{aligned} \tag{B.1}$$

# C Original figure concordance

Use the original figure identifier to locate the same image in the manuscript. The cart identification trace, the initial and optimized frequency plots, all Simulink time histories and the four-length comparison retain their original panels, axes and data annotations. The original cover sketch and executive-summary image are also retained.

**Table C.1** – Original figure and its location in the revised manuscript. Page numbers in the source column are physical PDF pages.

| Source identifier | Source p. | Subject | Open figure |
|---|---|---|---|
| Cover | 1 | Cart, sinusoid and RST feedback sketch | Figure 1.1 |
| Executive Summary | 3 | Conceptual platform and tracking illustration | Figure 1.2 |
| Fig. 2.1 | 8 | Closed-loop RST control architecture | Figure 2.1 |
| Fig. 3.1 | 11 | Cart–pendulum control architecture | Figure 3.1 |
| Fig. 3.2 | 12 | Cart-position servo-control diagram | Figure 3.2 |
| Fig. 3.3 | 13 | Cart identification response | Figure 3.3 |
| Fig. 3.4 | 14 | Cart-position and angle measurement | Figure 3.5 |
| Fig. 3.5 | 15 | Reduced architecture with cart servo | Figure 3.6 |
| Fig. 3.6 | 15 | Equivalent cascade | Figure 3.7 |
| Fig. 4.1 | 17 | Reduced RST synthesis loop | Figure 4.1 |

**Table C.2** – Original figure and its location in the revised manuscript. Page numbers in the source column are physical PDF pages.

| Source identifier | Source p. | Subject | Open figure |
|---|---|---|---|
| Fig. 4.2 | 18 | Original pole-placement plot | Figure 4.2 |
| Fig. 4.3 | 19 | Initial target coefficients | Figure 4.4 |
| Fig. 4.4 | 19 | MATLAB solution for R and S | Figure 4.5 |
| Fig. 4.5 | 20 | MATLAB coefficients for T | Figure 4.6 |
| Fig. 5.1 | 21 | Initial margins | Figure 5.3 |
| Fig. 5.2 | 22 | Initial Bode plot | Figure 5.4 |
| Fig. 5.3 | 22 | Initial Nyquist plot | Figure 5.6 |
| Fig. 5.4 | 23 | Original Simulink model | Figure 6.1 |
| Fig. 5.5 | 23 | Initial tracking, error, command and angle | Figure 6.2 |
| Fig. 5.6 | 24 | Initial tracking close-up | Figure 6.3 |

**Table C.3** – Original figure and its location in the revised manuscript. Page numbers in the source column are physical PDF pages.

| Source identifier | Source p. | Subject | Open figure |
|---|---|---|---|
| Fig. 5.7 | 24 | Initial angle plot | Figure 6.4 |
| Fig. 6.1 | 26 | Optimized Bode plot | Figure 5.5 |
| Fig. 6.2 | 26 | Optimized Nyquist plot | Figure 5.7 |
| Fig. 6.3 | 27 | Optimized tracking, error, command and angle | Figure 6.5 |
| Fig. 6.4 | 27 | Optimized tracking close-up | Figure 6.6 |
| Fig. 6.5 | 27 | Optimized angle plot | Figure 6.7 |
| Fig. 7.1 | 28 | Four-length margin and command output | Figure 6.8 |
| Fig. 7.2 | 29 | Four-length reference, angle and command | Figure 6.9 |
| Fig. 7.3 | 29 | Four-length tracking close-up | Figure 6.10 |
| Fig. 7.4 | 30 | Four-length angle comparison | Figure 6.11 |

# D Original equations and numerical statements

The original display equations below retain the notation, rounding and intermediate lines of [1]. They are grouped by source page. The annotated source passages keep the historical versions of the signs and coefficient values. The derivation and numerical interpretation in the main text give the versions used in the expanded study.

The complete 37-page source PDF is attached to this document as *RST_Inverted_Pendulum_Report.pdf*. It preserves the full original text, including mathematical expressions in prose, the original cover, tables, captions and code layout. The attached file is a copy of [1].

**Source p. 2 Abstract parameters**

$42.8^{\circ}$, $\beta = 0.5$ and $\gamma = 30$, $\pm 5$ V, $17.56^{\circ}$ $15.05^{\circ}$.

$L \in \{0.16, 0.23, 0.28, 0.35\}$ m.

**Source p. 3 Executive Summary parameters**

$\pm 5$ V $42.8^{\circ}$, $\beta = 0.5$, $\gamma = 30$,

**Source p. 4 Nomenclature**

$$\alpha = \sqrt{g/l}$$

**Source p. 7 Design bounds**

$\pm 5$ V;

**Source p. 8 Sinusoidal steady state and plant transfer**

$$e(t) = A \sin(\omega_0 t),$$

$$\boxed{s(t) = A\,|G(i\omega_0)| \sin(\omega_0 t + \arg[G(i\omega_0)])}.$$

$$\boxed{|G(i\omega_0)| = 0}.$$

$$P(s) = \frac{B(s)}{A(s)}.$$

**Source p. 9 Reference and error channels, internal model and degrees**

$$\hat{y}(s) = \frac{B(s)T(s)}{A(s)S(s) + B(s)R(s)}\hat{r}(s),$$

$$\hat{e}(s) = \hat{y}(s) - \hat{r}(s).$$

$$\boxed{\hat{e}(s) = \frac{B(s)T(s) - A(s)S(s) - B(s)R(s)}{A(s)S(s) + B(s)R(s)}\hat{r}(s)}.$$

$$|B(i\omega_0)[T(i\omega_0) - R(i\omega_0)] - A(i\omega_0)S(i\omega_0)| = 0.$$

$$\boxed{T(i\omega_0) = R(i\omega_0) \quad \wedge \quad S(i\omega_0) = 0}.$$

$$\boxed{S(s) = \left(s^2 + \omega_0^2\right) F(s)}.$$

$$\deg R = k, \qquad \delta_0 = \text{relative degree}.$$

$$\boxed{R(s) = r_0 s^k + r_1 s^{k-1} + r_2 s^{k-2} + \cdots + r_k}.$$

$$\boxed{S(s) = s(s^2 + \omega_0^2)\left(s^{k+\delta_0-3} + \sigma_1 s^{k+\delta_0-4} + \cdots + \sigma_{k+\delta_0-3}\right)}.$$

$$A_{BF}(s) = A(s)S(s) + B(s)R(s),$$

$$\boxed{\deg A_{BF} = n + k + \delta_0}.$$

Additional expressions in the original text.

$r(t) = A\sin(\omega_0 t),$ $A(i\omega_0) \neq 0$ and $B(i\omega_0) \neq 0,$ $\pm i\omega_0$:

## Source p. 10 Coefficient count

$$\boxed{\operatorname{card}(\mathscr{R} \cup \mathscr{S}) = 2k + \delta_0 - 2}.$$

$$n + k + \delta_0 = 2k + \delta_0 - 2,$$

$$\boxed{k = n + 2}.$$

Additional expressions in the original text.

$n+k+\delta_0$ $2k+\delta_0-2$

## Source p. 11 Nonlinear equations, linearization and Laplace forms

The original angular sign and the printed denominator in the cart coupling are shown verbatim below. Section 3.2 derives the corrected forms used in the study.

$$\begin{cases} (M+m)\ddot{x} + ml\ddot{\theta}\cos\theta - ml\dot{\theta}^2\sin\theta = f, \\ \ddot{x}\cos\theta - g\sin\theta + l\ddot{\theta} = 0. \end{cases}$$

$$\begin{cases} f - (M+m)\ddot{x} = ml\ddot{\theta}, \\ l\ddot{\theta} = \ddot{x} - g\theta. \end{cases}$$

$$\begin{cases} f(s) - (M+m)s^2 X(s) = ml\,\theta(s), \\ ls^2\theta(s) = s^2 X(s) - g\theta(s). \end{cases}$$

$$\begin{cases} X(s) = \dfrac{1}{(M+m)s^2} f(s) - \dfrac{ml}{(M+m)s^2}\theta(s), \\ \theta(s) = \dfrac{s^2}{g - ls^2} X(s). \end{cases}$$

Additional expressions in the original text.

$\theta = 0$

## Source p. 12 Cart blocks and closed-loop servo

$$\boxed{G_1(s) = \frac{1}{(M+m)s^2}}, \qquad \boxed{G_2(s) = -\frac{ml}{M+m}}, \qquad \boxed{G_3(s) = \frac{s^2}{g - ls^2}}.$$

$$u(s) = K_p[x_{mc}(s) - x_m(s)] - K_d K_3 v(s),$$

$$v(s) = \frac{K_m}{1 + \tau_m s} u(s),$$

$$x(s) = \frac{v(s)}{s}, \qquad x_m(s) = K_1 x(s).$$

$$\frac{x_m(s)}{x_{mc}(s)} = \frac{K_m K_p K_1}{\tau_m s^2 + (1 + K_m K_d K_3)s + K_m K_p K_1}.$$

$$\boxed{H_1(s) = \frac{1}{\dfrac{\tau_m}{K_m K_p K_1} s^2 + \dfrac{1 + K_m K_d K_3}{K_m K_p K_1} s + 1}}.$$

$$H_1(s) = \frac{1}{\dfrac{s^2}{\omega_{0c}^2} + \dfrac{2\xi}{\omega_{0c}} s + 1},$$

$$\omega_{0c} = \sqrt{\frac{K_m K_p K_1}{\tau_m}},$$

## Source p. 13 Damping, static gain and successive peaks

$$\frac{2\xi}{\omega_{0c}} = \frac{1 + K_m K_d K_3}{K_m K_p K_1}, \qquad \xi = \frac{1 + K_m K_d K_3}{2K_m K_p K_1}\sqrt{\frac{K_m K_p K_1}{\tau_m}}.$$

$$G_{\text{static}} = \frac{\lim_{t\to+\infty} x_m(t)}{x_{mc}} = \frac{0.25}{0.25}, \qquad \boxed{G_{\text{static}} = 1}.$$

$$D_{\%} = \frac{|y_{\max\,/\,\min} - y_\infty|}{y_\infty} \times 100,$$

$$d_{1\%} = \frac{0.31 - 0.25}{0.25} \times 100 = 24\%, \qquad d_{2\%} = \frac{|0.24 - 0.25|}{0.25} \times 100 = 4\%.$$

$$\frac{d_2}{d_1} = \exp\left(-\frac{\pi\xi}{\sqrt{1-\xi^2}}\right),$$

$$\xi = \frac{-\ln(d_{2\%}/d_{1\%})}{\sqrt{\pi^2 + \ln^2(d_{2\%}/d_{1\%})}}, \qquad \omega_{0c} = \frac{\pi}{\sqrt{1-\xi^2}}\frac{1}{t_2 - t_1}.$$

Additional expressions in the original text.

$$f = 1.5\ \text{Hz} \qquad A_c = 0.5\ \text{V} \qquad x_{mc} = \pm 0.25\ \text{V}.$$

### Source p. 14 Sensing gains and pendulum transfer

$$\boxed{\xi \approx 0.495}, \qquad \boxed{\omega_{0c} \approx 51.66\ \text{rad s}^{-1}}.$$

$$y(s) = x(s) + l\theta(s).$$

$$y_m(s) = K_1 x(s) + aK_2\theta(s).$$

$$\begin{cases} \lambda = K_1, \\ \lambda l = K_2 a, \end{cases}$$

$$\boxed{\lambda = K_1}, \qquad \boxed{a = \frac{K_1}{K_2} l}.$$

$$G_3(s) = \frac{s^2}{g - ls^2} = \frac{s^2/l}{g/l - s^2}.$$

$$\omega_{0b} = \sqrt{\frac{g}{l}}.$$

Additional expressions in the original text.

$$t_1 = 1.41\ \text{s} \qquad t_2 = 1.48\ \text{s}, \qquad y_m(s) = \lambda y(s). \qquad \pm\sqrt{g/l}$$

### Source p. 15 Natural frequencies and cart-to-angle relations

The source writes the sensor expression with $x_m$ and $\theta_m$ here. Section 3.5 defines the physical and scaled variables used consistently in the expanded analysis.

| $l$ (m) | $\omega_{0b}$ (rad s$^{-1}$) |
|---|---|
| 0.16 | 7.83 |
| 0.23 | 6.53 |
| 0.28 | 5.92 |
| 0.35 | 5.29 |

$$y_m = K_1 x_m + aK_2\theta_m.$$

$$y_m = K_1(x + l\theta) = K_1 y.$$

$$x_m = H_1(s)x_{mc}, \qquad x = \frac{H_1(s)x_{mc}}{K_1},$$

$$\theta = G_3(s)x = G_3(s)\frac{H_1(s)x_{mc}}{K_1}.$$

Additional expressions in the original text.

$$g = 9.81\ \text{m s}^{-2} \qquad \omega_{0b} < \omega_{0c} \qquad a = K_1 l/K_2,$$

### Source p. 16 Equivalent reduced transfer and time constant

$$y_m = H_1(s)x_{mc}[1 + lG_3(s)].$$

$$1 + lG_3(s) = 1 + l\frac{s^2}{g - ls^2} = \frac{g}{g - ls^2}.$$

$$\tau = \sqrt{\frac{l}{g}} = \frac{1}{\alpha},$$

$$\frac{g}{g - ls^2} = \frac{1}{1 - \tau^2 s^2} = \frac{1}{(1 - \tau s)(1 + \tau s)}.$$

$$\frac{y_m}{x_{mc}} = H_1(s)H_2(s),$$

$$\boxed{H_2(s) = \frac{1}{(1 + \tau s)(1 - \tau s)}, \qquad \tau = \sqrt{\frac{l}{g}} = \frac{1}{\alpha}}.$$

### Source p. 17 Reduced model and controller degrees

$$H_2(s) = \frac{1}{(1 + \tau s)(1 - \tau s)} = \frac{-\alpha^2}{s^2 - \alpha^2} = \frac{B(s)}{A(s)},$$

$$\boxed{B(s) = -\alpha^2}, \qquad \boxed{A(s) = s^2 - \alpha^2}.$$

$$k = 4, \qquad \deg A_{BF} = 2n + 2 + \delta_0.$$

$$\boxed{R(s) = r_0 s^4 + r_1 s^3 + r_2 s^2 + r_3 s + r_4}.$$

$$\boxed{S(s) = s(s^2 + \omega_0^2)(s + \sigma_1)}.$$

Additional expressions in the original text.

$$\pm i\omega_0 \qquad n = \deg A = 2. \qquad k = n + 2, \qquad \delta_0 = 0$$

$$(\beta, \gamma) \in (\mathbb{R}^+)^2 \qquad -\beta \qquad -\gamma \qquad \{-\alpha, +\alpha\};$$

$$\{0, -i\omega_0, +i\omega_0\}; \qquad -\gamma$$

### Source p. 18 Target poles and initial numerical coefficients

$$\boxed{\mathcal{P}_{BF} = \{-\gamma, -\alpha, -\alpha, -\beta, -\beta - i\omega_0, -\beta + i\omega_0\}}.$$

$$A_{BF}(s) = (s+\gamma)(s+\alpha)^2(s+\beta)(s+\beta+i\omega_0)(s+\beta-i\omega_0).$$

$$\beta = 1, \qquad \gamma = 10, \qquad L = 0.35 \text{ m}.$$

$$A_{BF}(s) = s^6 + c_1 s^5 + c_2 s^4 + c_3 s^3 + c_4 s^2 + c_5 s + c_6,$$

$$c_1 = 23.5884, \qquad c_2 = 199.6778, \qquad c_3 = 766.3771,$$
$$c_4 = 1417.6844, \quad c_5 = 1388.9681, \quad c_6 = 560.5714.$$

### Source p. 19 Bézout expansion and polynomial coefficients

The printed initial coefficient $r_2 = +51.58$ is retained as written. The Bézout identity and original MATLAB output give $r_2 = -51.58$, as shown in Section 4.3.

$$A_{BF}(s) = A(s)S(s) + B(s)R(s).$$

$$\begin{aligned} A_{BF}(s) =& (s^2-\alpha^2)s(s^2+\omega_0^2)(s+\sigma_1) \\ & - \alpha^2(r_0 s^4 + r_1 s^3 + r_2 s^2 + r_3 s + r_4). \end{aligned}$$

$$\begin{cases} \sigma_1 = c_1, \\ r_0 = \dfrac{\omega_0^2 - \alpha^2 - c_2}{\alpha^2}, \\ r_1 = \dfrac{c_1(\omega_0^2 - \alpha^2) - c_3}{\alpha^2}, \\ r_2 = -\dfrac{\alpha^2\omega_0^2 + c_4}{\alpha^2}, \\ r_3 = -\dfrac{\alpha^2 c_1 \omega_0^2 + c_5}{\alpha^2}, \\ r_4 = -\dfrac{c_6}{\alpha^2}. \end{cases}$$

$$\sigma_1 = 23.5884,$$
$$r_0 = -8.0884, \quad r_1 = -50.0895,$$
$$r_2 = 51.58, \qquad r_3 = -73.1438, \quad r_4 = -20.$$

$$\deg T(s) \le \deg S(s) = 4.$$

Additional expressions in the original text.

$$s^6 + c_1 s^5 + \cdots + c_6$$

### Source p. 20 Feedforward constraints and real coefficient system

$$T(s) = (s+\gamma)(s+\beta)(t_0 s^2 + t_1 s + t_2).$$

$$T(i\omega_0) = R(i\omega_0) \qquad \text{and} \qquad T(0) = R(0).$$

$$\begin{cases} (i+\gamma)(i+\beta)(-t_0 + it_1 + t_2) = r_0 - ir_1 - r_2 + ir_3 + r_4, \\ \gamma\beta t_2 = r_4. \end{cases}$$

$$\begin{pmatrix} 1-\gamma\beta & -(\gamma+\beta) \\ -(\gamma+\beta) & \gamma\beta - 1 \end{pmatrix} \begin{pmatrix} t_0 \\ t_1 \end{pmatrix} = \begin{pmatrix} r_0 - r_2 + r_4 - (\gamma\beta - 1)t_2 \\ r_3 - r_1 - (\gamma+\beta)t_2 \end{pmatrix},$$

$$\boxed{t_2 = \frac{r_4}{\gamma\beta}}.$$

$$\boxed{t_0 = -1.7912}, \qquad \boxed{t_1 = -2.3064}, \qquad \boxed{t_2 = -2}.$$

Additional expressions in the original text.

$$-\gamma \text{ and } -\beta \qquad \omega_0 = 1 \text{ rad s}^{-1}$$

### Source p. 21 Modulus margin

$$M_m = \min_{\omega} |1 + L(i\omega)|.$$

$$\omega_0^2. \text{ The}$$

Additional expressions in the original text.

$$-1: \qquad -20 \text{ dB/decade}, \qquad \omega = 1 \text{ rad s}^{-1} \qquad s^2 + \omega_0^2$$
$$\omega = 2.77 \text{ rad s}^{-1} \qquad 30^\circ \qquad -3.82 \text{ dB} \qquad \omega = 7.44 \text{ rad s}^{-1}$$
$$+\alpha \qquad P = 1, \qquad -1. \qquad -1.53 \qquad -1 \qquad N = P = 1,$$

### Source p. 23 Initial modulus-margin estimate

$$M_m \approx 0.49.$$

Additional expressions in the original text.

$$\beta = 1 \text{ and } \gamma = 10, \qquad [-5, 5] \text{ V}. \qquad t = 15 \text{ s}.$$

### Source p. 24 Angular excursion and nonlinear terms

$$20^\circ \qquad 17.56^\circ. \qquad ml\dot{\theta}^2 \sin\theta \qquad ml\ddot{\theta}\cos\theta$$

### Source p. 25 Retuning constraints and optimized phase margin

The source uses these rate inequalities as tuning guidance. Section 7 tests the margins with the cart servo retained.

$$\omega_{0b} = 5.29 \text{ rad s}^{-1} \qquad \text{and} \qquad \omega_{0c} = 51.66 \text{ rad s}^{-1}$$

$$0 < \beta \ll \omega_{0b} \ll \gamma \ll \omega_{0c}.$$

$$\beta \in (0, 5.29), \qquad \gamma \in (5.29, 51.66).$$

$$\boxed{\beta = 0.5}, \qquad \boxed{\gamma = 30},$$

$$\boxed{P_m = 42.8^\circ},$$

Additional expressions in the original text.

$\pm 5$ V $\omega_{0b} = 5.29$ rad s$^{-1}$ $40^\circ$ $+\alpha$ $[-5, 5]$ V.

### Source p. 27 Reported transient values

The source prose gives 15.05° for the optimized response. The original angular plot labels the time as 15.05 s and the angle as 14.3023°. See Section 6.3.

$17.56^\circ$ $15.05^\circ$.

### Source p. 28 Fixed controller and tested lengths

$$\beta = 0.5, \qquad \gamma = 30,$$

$$L \in \{0.16, 0.23, 0.28, 0.35\} \text{ m}.$$

Additional expressions in the original text.

$\alpha_k = \sqrt{g/L_k}$ $48^\circ$ $-\alpha$

### Source p. 30 Shortest pendulum and angular excursion

$+\alpha$ $31.33^\circ$. $L = 0.16$ m,

### Source p. 31 Original concluding values

$\omega_{0c} \approx 51.66$ rad s$^{-1}$ $\xi \approx 0.495$, $s^2 + \omega_0^2$.

$T(i\omega_0) = R(i\omega_0)$. $k = n + 2$, $A_{BF} = AS + BR$

$\pm 5$ V $42.8^\circ$. $\beta = 0.5$ and $\gamma = 30$ $17.56^\circ$

$15.05^\circ$. $L = 0.16, 0.23, 0.28,$ $31.33^\circ$. $H_\infty$.

# E Original MATLAB listings

The six MATLAB extracts are reproduced from [1], Appendix A. The original numbering identifies each source line. Indented display continuations belong to the preceding numbered line. The original project names *TP2_RST_Pendule_Dev_KUMAR.m*, *simu_rst_pendule.mdl* and *placement_poles.py*.

### Source listing A.1 Closed-loop pole assignment and polynomial coefficients

Original PDF p. 32.

```
1      %% Closed-loop polynomial
2      l = 0.35;
3      g = 9.81;
4      alpha = sqrt(g/l);
5      beta = 1;
6      gamma = 10;
7      omega0 = 1;
8
9      Abf = poly([-alpha; -alpha; -beta;
     -gamma; ...
10                     -beta-1i*omega0;
     -beta+1i*omega0]);
11
12     c1 = Abf(2);
13     c2 = Abf(3);
14     c3 = Abf(4);
15     c4 = Abf(5);
16     c5 = Abf(6);
17     c6 = Abf(7);
18
19     fprintf(['c1=%.4f c2=%.4f c3=%.4f
     c4=%.4f ' ...
20              'c5=%.4f c6=%.4f\n'],
     c1,c2,c3,c4,c5,c6)
```

### Source listing A.2 Bézout-equation coefficient identification

Original PDF p. 32.

```
1      %% R and S polynomials
2      sigma1 = c1;
3      r0 = (omega0^2-alpha^2-c2)/alpha^2;
4      r1 = (c1*(omega0^2-alpha^2)-c3)/alpha^2;
5      r2 = -(alpha^2*omega0^2+c4)/alpha^2;
6      r3 = -(alpha^2*c1*omega0^2+c5)/alpha^2;
7      r4 = -c6/alpha^2;
8
9      fprintf('sigma1=%.4f\n', sigma1)
10     fprintf('r0=%.4f r1=%.4f r2=%.4f r3=%.4f
     r4=%.4f\n', ...
11             r0,r1,r2,r3,r4)
```

### Source listing A.3 Feedforward-polynomial calculation

Original PDF p. 33.

```
1   %% T polynomial
2   t2 = r4/(gamma*beta);
3   M = [1-gamma*beta, -(gamma+beta); ...
4        -(gamma+beta), gamma*beta-1];
5   Y = [r0-r2+r4-(gamma*beta-1)*t2; ...
6        r3-r1-(gamma+beta)*t2];
7   Sol = M\Y;
8   t0 = Sol(1);
9   t1 = Sol(2);
10
11  fprintf('t0=%.4f t1=%.4f t2=%.4f\n',
     t0,t1,t2)
```

### Source listing A.4 Frequency-domain stability calculations

Original PDF p. 33.

```
%% Controller analysis
R_o = [r0_o, r1_o, r2_o, r3_o, r4_o];
S_o = conv([1 0 1 0], [1 sigma1_o]);
T_o = conv([1 beta_opt+gamma_opt
 beta_opt*gamma_opt], ...
              [t0_o t1_o t2_o]);
A_o = [1, 0, -alpha^2];
B_o = -alpha^2;
num_BO_o = conv(B_o, R_o);
den_BO_o = conv(S_o, A_o);

[Gm_o, Pm_o, Wcg_o, Wcp_o] =
 margin(num_BO_o, den_BO_o);
[re_o, im_o, ~] = nyquist(tf(num_BO_o,
 den_BO_o));

re_o = squeeze(re_o);
im_o = squeeze(im_o);
Mm_o = min(sqrt((re_o+1).^2 + im_o.^2));

fprintf('\nStability margins:\n')
fprintf(' Gain margin: %.4f dB\n',
 20*log10(Gm_o))
fprintf(' Phase margin: %.4f deg\n', Pm_o)
fprintf(' Modulus margin: %.4f\n', Mm_o)
fprintf(' Gain crossover frequency: %.4f
 rad/s\n', Wcg_o)
fprintf(' Phase crossover frequency: %.4f
 rad/s\n', Wcp_o)
```

## Source listing A.5 Optimized frequency- and time-domain evaluation

Original PDF pp. 33–34.

```
%% Frequency plots - optimized RST
figure('Name','Optimized RST
 Bode','NumberTitle','off');
margin(num_BO_o, den_BO_o);
title('Open-loop Bode diagram - optimized
 RST (beta=0.5, gamma=30)')
grid on;

figure('Name','Optimized RST
 Nyquist','NumberTitle','off');
nyquist(num_BO_o, den_BO_o);
title('Open-loop Nyquist diagram -
 optimized RST (beta=0.5, gamma=30)')
  axis([-2 0.5 -2 2]); grid on; hold on;
  theta_circle = linspace(0,2*pi,200);
  plot(-1 + Mm_o*cos(theta_circle),
 Mm_o*sin(theta_circle), ...
       'r--','LineWidth',1.5)
  plot(-1,0,'r+','MarkerSize',12,'LineWidt
 h',2)
  legend('Open-loop Nyquist', ...
         sprintf('Modulus-margin circle
 M_m = %.3f',Mm_o), ...
         'Critical point
 -1','Location','best')
  hold off;

  %% Simulink simulation - optimized RST
  beta = beta_opt;
  gamma = gamma_opt;
  sigma1 = sigma1_o;
  r0 = r0_o; r1 = r1_o; r2 = r2_o; r3 =
 r3_o; r4 = r4_o;
  t0 = t0_o; t1 = t1_o; t2 = t2_o;
  R = R_o; S = S_o; T = T_o;
  H = poly([-2 -2 -1 -1]);
  sim('simu_rst_pendule')

  figure('Name','Optimized RST time
response','NumberTitle','off');
  subplot(4,1,1)
  plot(t,ymc,'g','LineWidth',1.5); hold on
  plot(t,ym,'r','LineWidth',1.2)
  legend('Reference y_{mc}','Output
y_m','Location','best')
  xlabel('Time (s)'); ylabel('Position
(V)')
  title('Reference tracking - optimized
RST (beta=0.5, gamma=30)')
  ylim([-3 3]); grid on

  subplot(4,1,2)
  plot(t,ym-ymc,'c','LineWidth',1.2)
  xlabel('Time (s)'); ylabel('Error (V)')
  title('Tracking error e(t) =
y_m(t)-y_{mc}(t)'); grid on

  subplot(4,1,3)
  plot(t,u,'m','LineWidth',1.2); hold on
  yline(5,'r--','+5 V limit');
yline(-5,'r--','-5 V limit')
  xlabel('Time (s)'); ylabel('Command u
(V)')
  title('Control command u(t)'); ylim([-7
7]); grid on

  subplot(4,1,4)
  plot(t,Theta,'Color',[1 0.5
0],'LineWidth',1.2)
  xlabel('Time (s)'); ylabel('Angle theta
(deg)')
  title('Pendulum angle theta(t)'); grid
on
```

## Source listing A.6 Parametric robustness analysis

Original PDF pp. 34–35.

```
  %% Robustness test: pendulum-length
variation
  L_values = [0.16, 0.23, 0.28, 0.35];
  colors = {'r','b','m','c'};
  l_original = l;
  results_t = cell(length(L_values),1);
  results_ymc = cell(length(L_values),1);
  results_ym = cell(length(L_values),1);
  results_u = cell(length(L_values),1);
  results_th = cell(length(L_values),1);

fprintf('\n========== ROBUSTNESS TEST -
  Variation of L ==========\n')
fprintf('(Fixed optimized RST: beta=%.2f,
  gamma=%.2f)\n\n', ...
```

```
        beta_opt,gamma_opt)
fprintf('%-10s %-10s %-15s %-15s %-15s %-12s\n', ...
        'L (m)','alpha','Gm (dB)','Pm (deg)','Mm','|u|max (V)')

for k = 1:length(L_values)
    l = L_values(k);
    alpha_k = sqrt(g/l);
    A_k = [1,0,-alpha_k^2];
    B_k = -alpha_k^2;
    num_BO_k = conv(B_k,R_o);
    den_BO_k = conv(S_o,A_k);
    [Gm_k,Pm_k,~,~] = margin(num_BO_k,den_BO_k);
    [re_k,im_k,~] = nyquist(tf(num_BO_k,den_BO_k));
    re_k = squeeze(re_k); im_k = squeeze(im_k);
    Mm_k = min(sqrt((re_k+1).^2 + im_k.^2));
    sim('simu_rst_pendule')
    results_t{k} = t;
    results_ymc{k} = ymc;
    results_ym{k} = ym;
    results_u{k} = u;
    results_th{k} = Theta;
    fprintf('%-10.2f %-10.4f %-15.4f %-15.4f %-15.4f %-12.4f\n', ...
            l,alpha_k,20*log10(Gm_k),Pm_k,Mm_k,max(abs(u)))
end

l = l_original;

labels_ym = arrayfun(@(L) sprintf('y_m (L=%.2f m)',L), ...
    L_values,'UniformOutput',false);
labels_th = arrayfun(@(L) sprintf('theta (L=%.2f m)',L), ...
    L_values,'UniformOutput',false);
labels_u = arrayfun(@(L) sprintf('u (L=%.2f m)',L), ...
    L_values,'UniformOutput',false);

figure('Name','Robustness test - variation of L','NumberTitle','off')
subplot(3,1,1)
plot(results_t{1},results_ymc{1},'g','LineWidth',1.8); hold on
for k=1:length(L_values)
    plot(results_t{k},results_ym{k},colors{k},'LineWidth',1.2)
end
legend([{'Reference y_{mc}'},labels_ym],'Location','best')
xlabel('Time (s)'); ylabel('Position (V)')
title('Reference tracking - robustness to variation of L')
ylim([-3 3]); grid on

subplot(3,1,2); hold on
for k=1:length(L_values)
    plot(results_t{k},results_th{k},colors{k},'LineWidth',1.2)
end
legend(labels_th,'Location','best')
xlabel('Time (s)'); ylabel('Angle theta (deg)')
title('Pendulum angle theta(t)'); grid on

subplot(3,1,3); hold on
for k=1:length(L_values)
    plot(results_t{k},results_u{k},colors{k},'LineWidth',1.2)
end
yline(5,'k--','+5 V limit'); yline(-5,'k--','-5 V limit')
legend(labels_u,'Location','best')
xlabel('Time (s)'); ylabel('Command u (V)')
title('Control command u(t)'); ylim([-7 7]); grid on
```